Title

Presynaptic NMDA receptors cooperate with local action potentials to implement activity-dependent GABA release from the reciprocal olfactory bulb granule cell spine

Authors

Vanessa Lage-Rupprecht[1,2], Li Zhou[1], Gaia Bianchini[1], S. Sara Aghvami[1,3,4], Balázs Rózsa[5], Marco Sassoé-Pognetto[6] & Veronica Egger[1*]

Affiliations

1. Neurophysiology, Institute of Zoology, Universität Regensburg, 93040 Regensburg, Germany; 2. Department of Bioinformatics, Fraunhofer SCAI, 53757 Sankt Augustin, Germany; 3. School of Electrical and Computer Engineering, University of Tehran, 14395-515 Tehran, Iran; 4. School of Cognitive Sciences, Institute for Research in Fundamental Sciences (IPM), 19395-5746 Tehran, Iran; 5. Two-Photon Imaging Center, Institute of Experimental Medicine, Hungarian Academy of Sciences, 1039 Budapest, Hungary; 6. Neuroscience Department, University of Turin, I-10126 Torino, Italy.

Abstract

In the rodent olfactory bulb the smooth dendrites of the principal glutamatergic mitral cells (MCs) form reciprocal dendrodendritic synapses with large spines on GABAergic granule cells (GC), where unitary release of glutamate can trigger postsynaptic local activation of voltage-gated Na^+-channels (Na_Vs), i.e. a spine spike. Can such single MC inputs evoke reciprocal release? We find that unitary-like activation via two-photon uncaging of glutamate causes GC spines to release GABA both synchronously and asynchronously onto MC dendrites. This release indeed requires activation of Na_Vs and high-voltage-activated Ca^{2+}-channels (HVACCs), but also of NMDA receptors (NMDAR). Simulations show temporally overlapping HVACC- and NMDAR-mediated Ca^{2+}-currents during the spine spike, and ultrastructural data prove NMDAR presence within the GABAergic presynapse. The cooperative action of presynaptic NMDARs allows to implement synapse-specific, activity-dependent and non-topographical lateral inhibition and thus could provide an efficient solution to combinatorial percept synthesis in a sensory system with many receptor channels.

Introduction

Reciprocal dendrodendritic microcircuits can be found in several parts of the nervous system and are especially abundant in the vertebrate olfactory bulb (*Crespo et al. 2013*), where the dendrites of the principal mitral and tufted cells (MTCs) engage in such interactions with several major subtypes of local GABAergic neurons. In the glomerular layer, the MTC apical tuft is reciprocally connected to mostly periglomerular cell dendrites. In the external plexiform layer, the long MC lateral dendrites are densely covered with GABAergic synapses that mostly originate from reciprocal arrangements (*Bartel et al. 2015; Sailor et al. 2016; Matsuno et al. 2017*). While proximal circuits are thought to be mostly formed by granule cell (GC) spines (*Miyamichi et al. 2013*), there are also reciprocal dendrodendritic interactions with other GABAergic cell types such as SOM+ neurons, CRH+ neurons and most prominently parvalbumin/PV+ neurons that all feature aspiny, smooth dendrites (partially overlapping populations; *Toida et al. 1994; Lepousez et al. 2010; Huang et al. 2013; Kato et al. 2013; Miyamichi et al. 2013)*.

Thus the MC-GC synapse differs from the other bulbar reciprocal arrangements by its location within a large spine on the GC side. These spines feature particularly long necks (*Woolf et al. 1991*) which might serve to electrically isolate the synapse and boost local

processing (e.g. *Miller et al. 1985; Spruston 2008*). Indeed, we have gathered evidence that unitary postsynaptic potentials in GC spines are electrically compartmentalized and thus can locally activate voltage-gated Na^+-channels (Na_vs) which in turn activate classic presynaptic high-voltage activated Ca^{2+}-channels (HVACCs) within the spine ('spine spike', *Bywalez et al. 2015*). Thus, the reciprocal spine might operate as a mini-neuron that can generate synaptic output upon local activation (*Egger & Urban 2006*).

While there have been many earlier studies of recurrent dendrodendritic inhibition at the MTC-GC synapse, it is so far unknown whether a unitary, purely local activation of the spine's microcircuit can indeed trigger release of GABA back onto the exciting MTC. The issue is still unresolved because (1) paired recordings of synaptically coupled GCs and MTCs are notoriously hard to perform (e.g. *Pressler & Strowbridge 2017;* see also Discussion) and would also not allow to fully dissect the circuit, and (2) most earlier studies used a strong stimulation of voltage-clamped MCs, namely a depolarization to 0 mV for 20-50 ms *(Isaacson & Strowbridge 1998; Halabisky et al. 2000; Isaacson 2001; Chen et al. 2000*). This protocol will cause massive release of glutamate from the lateral MC dendrites, invoking glutamate spillover between them (*Isaacson 1999*) and resulting in long-lasting recurrent inhibition of MCs with both synchronous and asynchronous components, the latter with a time constant of ~ 500 ms. Under these circumstances and zero extracellular $[Mg^{2+}]_e$ GC NMDA receptor (NMDAR) activation was shown to be an important source of Ca^{2+} entry that suffices to trigger release of GABA from the GC spine (also in *Schoppa et al. 1998*). However, in normal $[Mg^{2+}]_e$ GABA release was mostly abolished by HVACC blockade (*Isaacson 2001*; see Discussion).

Here we aim to determine whether – and possibly how - single inputs from MC lateral dendrites to GC spines can also trigger recurrent release of GABA from the reciprocal synapse, using recordings from fluorescently labeled MCs and two-photon uncaging (TPU) of glutamate along their lateral dendrite near Venus-tagged GC spines. TPU of glutamate allows to study the activation of the reciprocal microcircuit in single GC spines without interfering with spine Na_v and HVACC channels or causing broader GC activation (*Bywalez et al. 2015*), which here also enables investigation of the reciprocal output by the GABAergic release machinery via recording of IPSCs in mitral cells in response to TPU at single GC

spines. Thus, processing within a single mini-neuron can be disentangled in space and time from broader extended activation, in order to test the main predictions from our previous study: The mini-neuron hypothesis along with the GC spine spike phenomenon suggest that just like in conventional axons, Na_v and ensuing HVACC activation are required to cause release, and that unitary activation of the spine is sufficient for triggering release.

While these notions could be confirmed, our study also reveals that presynaptic NMDARs can gate reciprocal output at the single-spine level. What is the advantage of such an arrangement compared to classical neuronal processing? In olfactory coding, a large number of input channels needs to be combined to synthesize an olfactory percept (e.g. *Mori et al. 1999, Murthy 2011*). We propose that the mechanisms revealed here allow reciprocal GC spines to play a central role in the efficient binding of changing sets of activated olfactory receptor channels.

Results

Experimental configuration

To enable pharmacological interference with components of the reciprocal microcircuit such as Na_vs and HVACCs, we bypassed release from the MC presynapse via TPU of DNI-caged glutamate (DNI, see Methods; *Chiovini et al. 2014; Bywalez et al. 2015; Palfi et al. 2018*) in acute juvenile rat olfactory bulb slices, while recording from MCs in somatic whole-cell voltage-clamp. To visualize the lateral dendrites, MCs were filled with the dye Alexa594 (50 µM). Fig. 1A shows the recording configuration.

In all MC recordings we observed a high basal frequency of spontaneous events which is a general hallmark of the olfactory bulb network *(Egger & Urban 2006*). Wash-in of 1 mM DNI further increased the basal frequency by on average 1.9 ± 1.2 times (mean value before DNI: 4.5 ± 2.1 Hz, n = 14, $P < 0.01$), due to the disinhibition resulting from a partial blockade of $GABA_A$Rs by DNI, which also reduced the mean spontaneous IPSC amplitude to a fraction of 0.47 ± 0.16 of control (n = 14 MCs, $P < 0.001$, Fig. S1A,B,C (attached at the end of the manuscript). In the presence of DNI, the $GABA_A$R antagonist bicuculline (BCC, 50 µM) blocked spontaneous activity almost completely (frequency: 0.13 ± 0.10 of control, n = 6, $P < 0.01$, Fig. 1C, Fig. S1A).

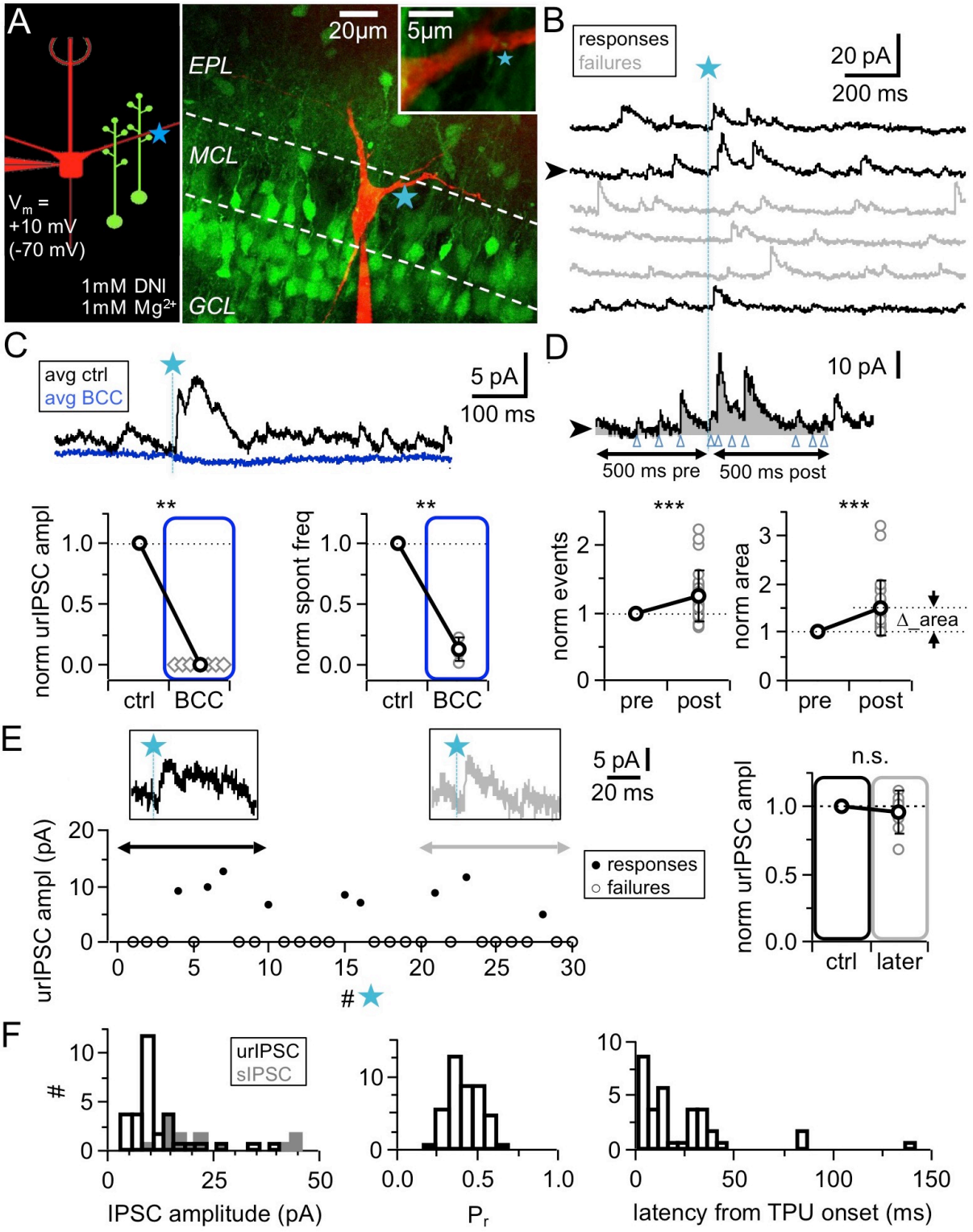

Figure 1. **TPU-induced glutamatergic activation of GC spines triggers GABA release detected as uncaging-evoked reciprocal IPSCs (urIPSCs) in MCs.**

(**A**) Experimental setting (scheme and image): Somatic whole cell voltage clamp recording from MC filled with Alexa 594 (red, 50 µM) and TPU of DNI-caged glutamate (DNI; blue star) at GC spines in VGAT-Venus rats (GCs green).

(**B**) Example of consecutive uncaging traces showing urIPSC responses (black) and failures (grey).

(**C**) Effect of $GABA_AR$ blockade (bicuculline, BCC, 50 µM, blue) on urIPSCs and spontaneous activity. Top: Example experiment, showing averaged traces. Bottom: Cumulative data on urIPSC amplitude (left panel, n =7) and on frequency of spontaneous events (right panel, n = 6).

(D) Analysis of asynchronous events. Top: Example trace from (B) with analysis intervals pre- and post-uncaging (grey areas, black arrows). Counted events marked by blue arrowheads. Bottom: Normalized IPSC event number and area (integrated activity, relative increase vs control Δ) in pre- versus post-uncaging intervals (n = 27, see Methods).

(**E**) Stability of urIPSC recordings. Left: Representative experiment showing individual urIPSC amplitude values over consecutive stimulations (1 TPU per min). Insets: Averaged urIPSC responses in the first (black, n = 3 responses) and last ten minutes (grey, n = 3). Right: Comparison of averaged normalized urIPSC amplitudes separated by 10 min interval (n = 7 MCs).
(**F**) Properties of first triggered urIPSCs. Left: Amplitudes (n = 32 MCs, V_m = +10 mV). Dark grey: Amplitude distribution of spontaneous IPSCs for comparison (n = 14 MCs, mean amplitudes). Middle: Release probabilities P_r (n = 44). Right: Latencies from TPU onset (n = 36).
All Figures: Significance (non-parametric tests): n.s. not significant, * $P < 0.05$, ** $P < 0.01$, *** $P < 0.001$; mean data ± S.D.

Since in initial experiments we occasionally observed activation of both NMDA and AMPA autoreceptors on MC dendrites at a holding potential of -70 mV, MCs were clamped to +10 mV in the main body of experiments, near the reversal potential of ionotropic glutamate receptors (*Isaacson 1999; Friedman & Strowbridge 2000*). All experiments were performed at physiological levels of $[Mg^{2+}]_e$ (1 mM).

Triggering of reciprocal IPSCs via TPU

To prevent overstimulation with glutamate, we uncaged with similar laser parameter settings as in the previous study (*Bywalez et al. 2015*), in which TPU-evoked GC Ca^{2+} signals were indistinguishable from those of unitary spontaneous or triggered synaptic inputs, and routinely tested these settings; to ensure similar laser power across experiments, uncaging sites were located at a shallow depth no more than 20 – 30 µm below the surface of the tissue (see Methods). In most experiments, uncaging was performed at one spot in the immediate vicinity of GC spines that were visible in VGAT-Venus rats and in close proximity (0.2 – 0.5 µm) to the MC lateral dendrite (e.g. Fig. 1A, 2A); in a few initial experiments in WT rats uncaging was performed 'blindly' at up to four spots along the dendrite to increase the likelihood for triggering a unitary response (e.g. Fig. 2B; 18% of experiments, see Methods). Responses were detectable in ~ 30% of tested MCs (total n = 166, see Methods) and in this fraction of MCs would occur only in a small subset of stimulations (see below, Fig. 1F), thus overstimulation of the circuit appears unlikely. All uncaging spots were located proximally, at distances < 50 µm from the MC soma (Fig. S1D). The rationale for this choice was to minimize electrotonic attenuation, since IPSC amplitudes were already small (see above, Fig. S1A,C). Moreover, proximal stimulation and the use of VGAT-Venus rats should prevent inadvertent stimulation of reciprocal synapses with other interneuron types (see Introduction).

TPU of glutamate resulted in consecutive triggered responses and failures in MCs (Fig. 1B). Responses were classified as triggered if they were observed repeatedly within the same time window and showed similar kinetics (see Methods). Next we tested whether these triggered responses were indeed GABAergic by applying the $GABA_AR$ antagonist Bicuculline (BCC, 50 µM), which invariably blocked responses completely (Fig. 1C, n = 7, P < 0.01, Wilcoxon test). Thus in the following the triggered events are denoted as urIPSCs (**u**ncaging-evoked **r**eciprocal IPSCs). Sufficient stability of such urIPSC responses was established via long-term recordings (see Methods). The mean amplitudes of responses during the first and last 5 -10 photostimulations (with at least 10 min in between to mimic the time course of pharmacological manipulations) were not significantly different (Fig. 1E, n = 7, ratio last to first 0.95 ± 0.15, P = 0.74).

The amplitude of triggered urIPSCs was on average 12 ± 8 pA, with a rise time of 6 ± 3 ms (in n = 32 MCs clamped to +10 mV), which is significantly smaller than the mean amplitudes of spontaneous IPSCs (n = 14; 22 ± 12 pA; P < 0.001, Mann-Whitney test, Fig. 1F). Since spontaneous IPSCs are highly likely to also originate from the reciprocal MC-GC circuit (see Discussion), this observation further argues against overstimulation with glutamate in our experiment. There was no detectable correlation between the urIPSC amplitude and the distance from the soma (n = 20, r = -0.07, Fig. S1D).

The average release probability from the reciprocal spine was estimated as P_r = 0.34 ± 0.11 (Fig. 1F, range 0.13 - 0.60, based on n = 44 MCs, see Methods and Discussion). The latencies of urIPSPCs were not normally distributed (Fig. 1F), with a first peak within the first 10 ms post TPU onset (n = 13), a second peak around 30 ms (n = 19 within the range 10-50 ms) and a yet more delayed tail (n = 3, see Fig. S1F and Discussion).

In most experiments we detected putative asynchronous urIPSCs following the first triggered event which were quantified via integral analysis and counting of events (Fig. 1D, see Methods and Discussion). Both area and number of events increased highly significantly in the 500 ms interval following TPU ('post') compared to the same interval right before ('pre'; mean increase of integrated activity Δ_area + 0.50 ± 0.55 relative to 'pre' value; mean increase in event number + 0.25 ± 0.37 relative to 'pre' value; n = 27, P < 0.001 for both; absolute values in 'pre' area 2.40 ± 1.83 pAs, event numbers 26.1 ± 14.9). Δ_area was also

significantly increased if the extra area of the synchronous urIPSC was subtracted ($P < 0.005$). The total duration of recurrent inhibition was on average 179 ± 137 ms (range 32 – 533 ms, n = 26, Fig. S1E). Thus, asynchronous recurrent inhibition can be already triggered by single glutamatergic inputs.

From all these experiments we conclude that local, unitary-like TPU of glutamate can indeed trigger both fast and slow reciprocal release of GABA, providing proof that the reciprocal microcircuit can be activated by single synaptic inputs at physiological levels of Mg^{2+}.

mean data ± S.D.

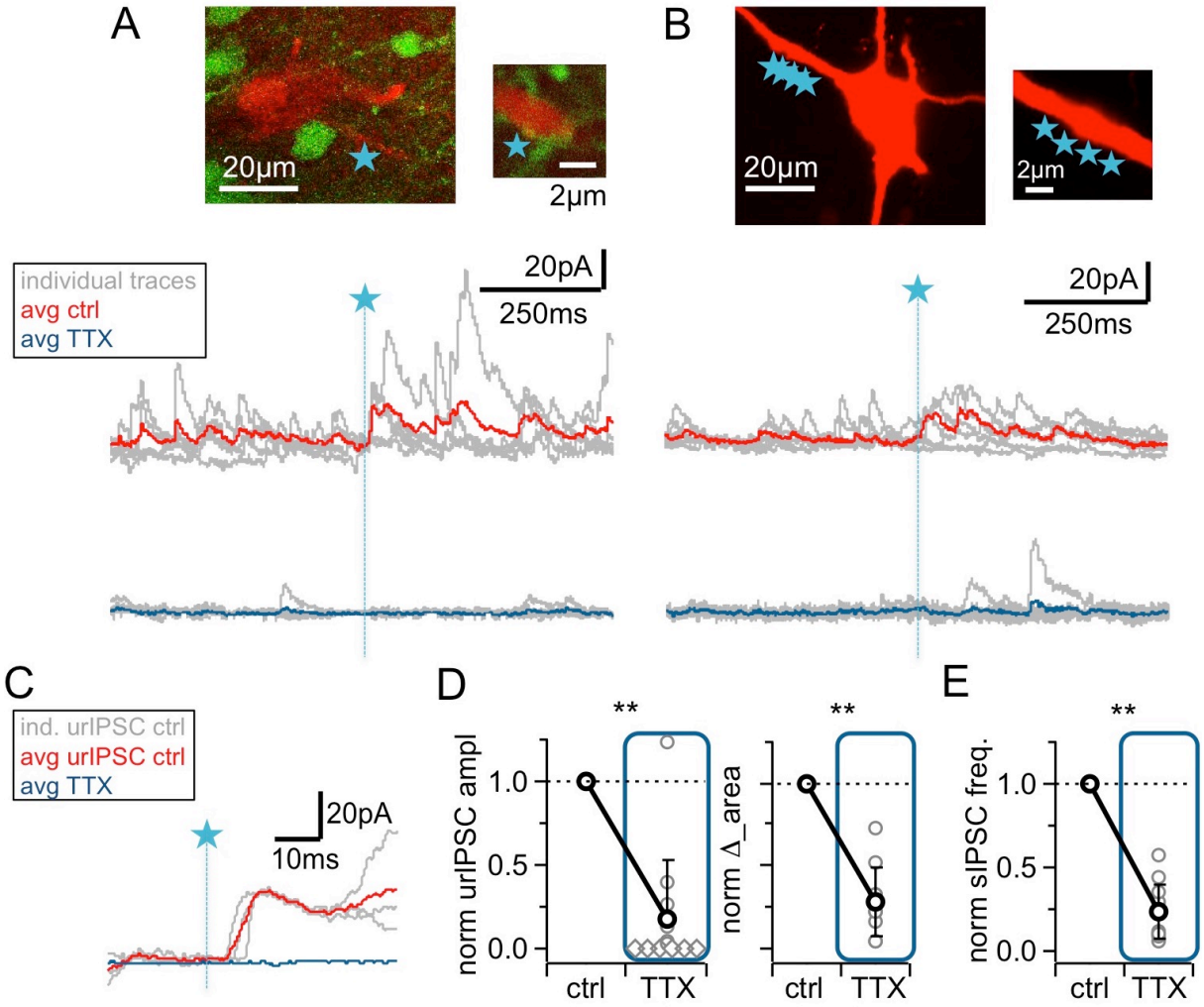

Figure 2. The urIPSC is reduced by Na_v blockade (TTX, 500 nM).
(**A, B**) Representative experiments showing a patch-clamped mitral cell (Alexa594 50 µM, red), the uncaging site(s) along a lateral dendrite (blue star) and below the corresponding uncaging traces with individual traces shown in grey, average control traces in red and average TTX traces indicated in blue (A: VGAT-Venus rat, single-site TPU, B: Wistar rat, multi-site TPU).
(**C**) Magnified illustration of traces in (A) (for control individual traces with urIPSC responses and their average, for TTX only average, color coding as above).
(**D**) Left: Cumulative normalized data showing the strong reduction of urIPSC amplitude during Na_v blockade with TTX (n = 12). Diamonds indicate the experiments with no detectable response in the presence of the drug. Right: Comparison of normalized IPSC Δ_area between control and in the presence of TTX (see Methods, n = 10).
(**E**) sIPSC frequency comparison beween control and in presence of TTX (n = 10). See also A,B.

Sodium channel activation is required for most urIPSCs

Next, we investigated a possible contribution of the GC spine spike and thus Na_v activation to urIPSC generation. Fig. 2 illustrates that wash-in of TTX (500 nM) substantially reduced both triggered and spontaneous events. On average, urIPSC amplitudes were reduced to a fraction of 0.17 ± 0.34 of control (Fig. 2D, n = 12, P < 0.005; absolute control amplitudes for -70 mV: -7.8 ± 3.6 pA, n = 5; for 10 mV: 15.4 ± 12.4 pA, n = 7), and the increase in integrated activity Δ_area was decreased to 0.28 ± 0.21 of its control value (see Methods; n = 10, P <

0.005). The frequency of spontaneous IPSCs (sIPSC) was also strongly decreased in TTX, to a fraction of 0.24 ± 0.17 of control (Fig. 2E, n = 10, P < 0.005).

Thus Na_vs are essential to trigger GABA release from the reciprocal spines.

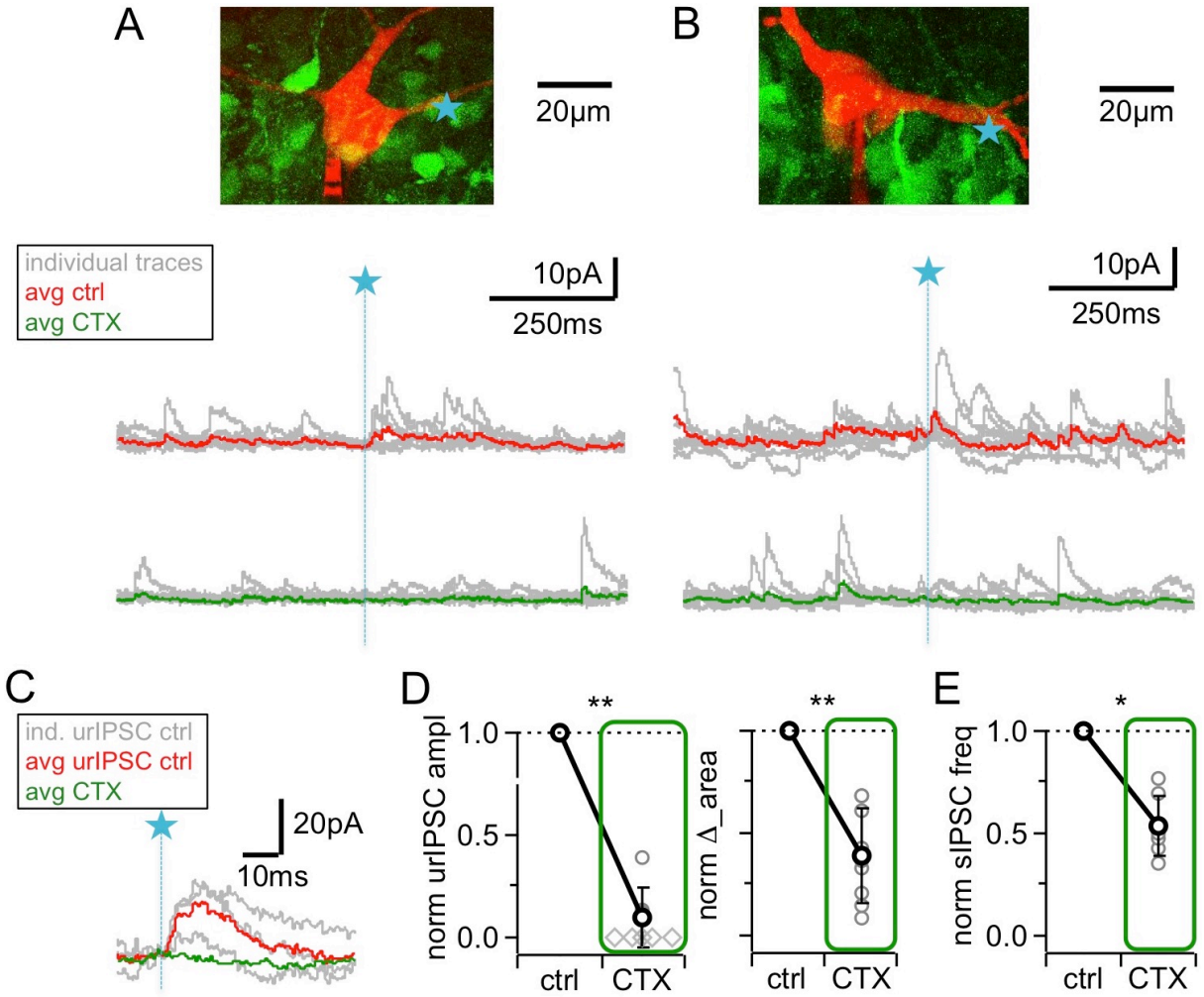

Figure 3. Blockade of high voltage activated Ca^{2+}-channels by ω-conotoxin MVIIC (CTX, 1 µM) causes a prominent reduction of urIPSC amplitudes.
(**A, B**) Two representative experiments in brain slices from VGAT-Venus rat with the corresponding MC (red), the site of TPU (blue star) and the uncaging traces according to the condition (individual traces : grey, average control: red, average CTX: green).
(**C**) Left: Magnified illustration of traces in B (for control individual traces with urIPSC responses and their average, for CTX only average, color coding as above).
(**D**) Left: Summary of effects of CTX on average normalized urIPSC amplitude (n = 8). Diamonds indicate the experiments with no detectable response in the presence of the drug. Right: Comparison of delta urIPSC areas normalized to control versus in the presence of CTX (n = 9).
(**E**) Inhibitory effect of CTX on spontaneous IPSC frequency (n = 7). See also A,B.

High-voltage activated Ca^{2+} channels in the spine trigger GABA release

HVACCs have been implied to mediate recurrent release from reciprocal spines (*Isaacson 2001*) and are activated by Na_vs, contributing a substantial fraction to the total postsynaptic Ca^{2+} signal in the GC spine (*Bywalez et al. 2015*). To directly test whether HVACC activation is required for release of GABA, we blocked NPQ-type Ca^{2+} channels with 1 µM ω-conotoxin MVIIC (CTX; *Bloodgood & Sabatini 2007; Bywalez et al. 2015*).

Fig. 3 shows the resulting substantial decrease of urIPSCs, to a fraction of 0.08 ± 0.14 of control (from a mean amplitude of 11.3 ± 5.7 pA; n = 8, P < 0.005, Fig. 3D). This decrease was not different from the effect of TTX on urIPSC amplitude described above (P = 0.35, ratios in CTX vs TTX). ∆_area decreased to 0.39 ± 0.23 of control (n = 9, P < 0.005, Fig. 3D), again statistically not different from the effect of TTX on ∆_area described above (P = 0.15 vs TTX).

CTX decreased sIPSC frequency to a fraction of 0.53 ± 0.15 of control, less markedly than TTX (Fig. 3E, n = 7 cells, control vs CTX: P < 0.01; CTX vs TTX: P < 0.005).

We conclude that HVACC activation is required for release of GABA from the reciprocal spine following local input.

NMDA receptors are also relevant for recurrent release

NMDARs are known to substantially contribute to unitary synaptic transmission and to postsynaptic Ca^{2+} entry at the MC to GC synapse (*Isaacson & Strowbridge 1998; Schoppa et al. 1998; Isaacson 2001; Egger et al. 2005*). However, because NMDAR-mediated Ca^{2+} entry into GC spines did not depend on Na_v activation in our previous study (in contrast to HVACC-mediated Ca^{2+} entry, *Bywalez et al. 2015*), and because of the strong blocking effects of TTX or CTX on urIPSCs reported above, we hypothesized that NMDAR blockade would have only mild effects on fast recurrent release upon single inputs. Intriguingly however, Fig. 4 shows that the application of 25 µM D-APV resulted in a substantial decrease of urIPSC amplitudes, to on average 0.22 ± 0.21 of control (from a mean amplitude of 13.8 ± 8.6 pA, n = 10, P < 0.002, Fig. 4D). All individual experiments showed the amplitude decrease, albeit to a variable degree (range 0.00 - 0.68 of control). ∆_area following TPU decreased to 0.40 ± 0.28 of control (n = 10, P < 0.003, Fig. 4D). Both effects were statistically not different from the effects of either TTX or CTX (amplitude: P = 0.12 and P = 0.08; ∆_area: P = 0.19 and P = 0.47).

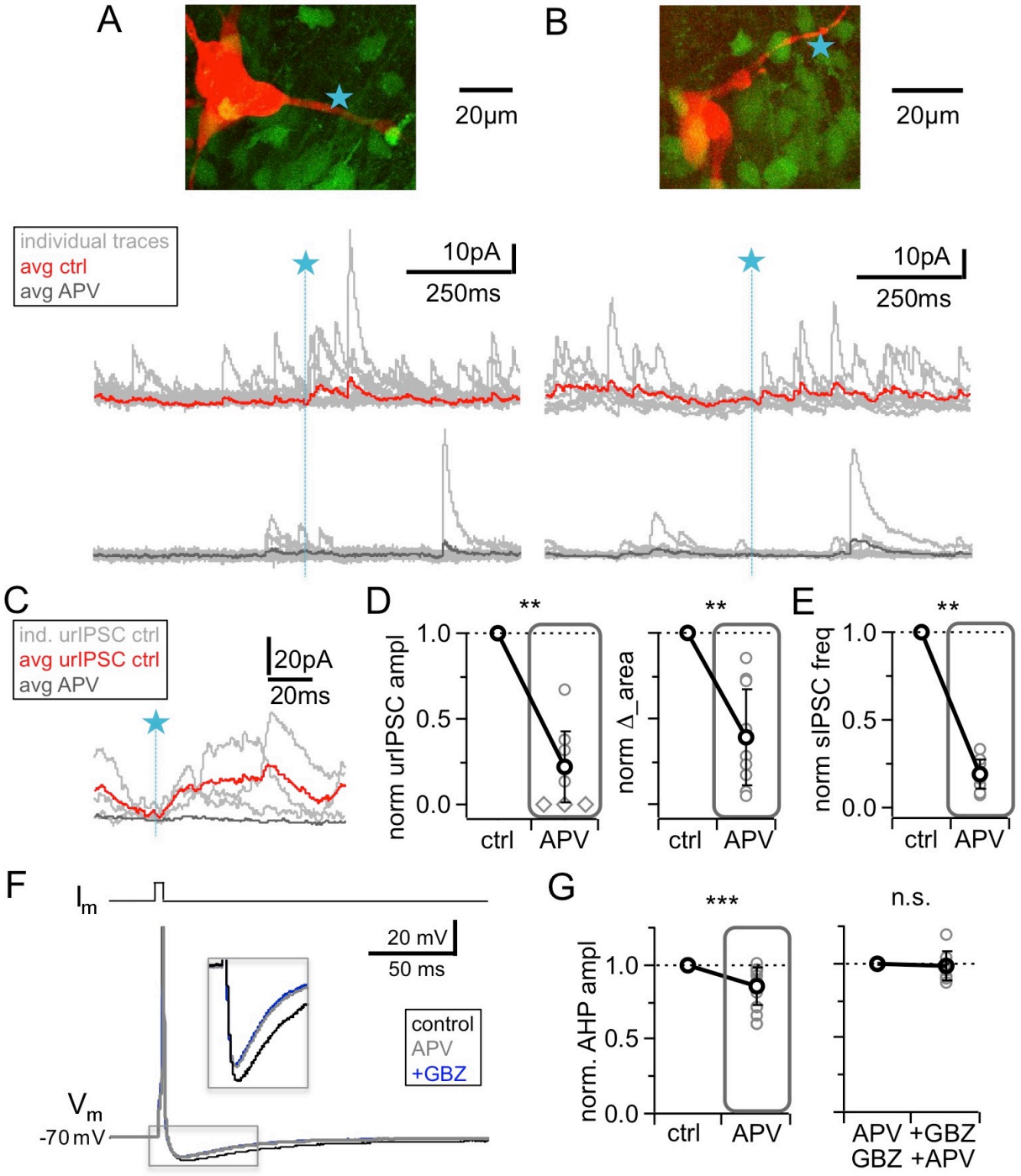

Figure 4. NMDAR blockade with D-APV (25 µM) results in a strong reduction of urIPSC amplitudes and also reduces AHPs following mitral cell APs

(**A, B**) Two representative uncaging experiments with the corresponding MC (red), the site of TPU (blue star) and the uncaging traces according to the condition (individual traces: grey, average control: red, average APV: dark grey); both VGAT-Venus.

(**C**) Magnified illustration of traces in A (for control individual traces with urIPSC responses (grey) and their average (red), for APV only average (dark grey)).

(**D**) Left: Summary of effects of APV on average normalized urIPSC amplitude (n = 10). Diamonds indicate the experiments with no detectable response in the presence of the drug. Right: Comparison of delta urIPSC integrals between control versus in the presence of APV (n = 10).

(**E**) Cumulative effect of APV on spontaneous IPSC frequency; see also A,B (n = 9).

(**F**) Representative example of MC AP evoked by somatic current injection in control conditions (black trace) and in the presence of APV (grey trace) and added GBZ (20 µM; blue trace). Inset: Magnified AHPs.

(**G**) Left: Cumulative effects of APV on average normalized AHP amplitude (n = 11 MCs). Right: Effect of occlusion experiments on AHP amplitude (APV before GBZ or GBZ before APV, n = 8).

APV also substantially reduced sIPSC frequency, to 0.19 ± 0.08 of control (n = 9, P < 0.01, Fig. 4E), similar to TTX (P = 0.84) and significantly more pronounced than CTX (P < 0.001). Since the strength of the effect of NMDAR blockade on urIPSCs was surprising to us, we sought to provide another line of evidence for these findings in an experimental setting that does not involve uncaging of glutamate (which might preferentially activate NMDARs, see Discussion). The afterhyperpolarization (AHP) following single MC APs elicited by somatic current injection was found to mainly reflect recurrent inhibition in brain slices from adult mouse (*Nunes & Kuner 2018*), while in juvenile rat inhibitory synaptic contributions to the AHP were observed to be less substantial but still detectable (on the order of 20-30% relative to the K^+ channel-mediated component, *Dumenieu et al. 2015*). We used this paradigm to test whether NMDAR blockade alone could interfere with recurrent inhibition (Fig. 4F, G). Single MC AP AHPs (n = 13 MCs, V_{hold} = -70 mV) had a mean amplitude ΔV_m = – 9.5 ± 2.1 mV and a mean half duration $t_{1/2}$ = 43 ± 25 ms. Fig. 4G shows that APV application significantly reduced the mean AHP amplitude to a fraction of 0.86 ± 0.12 of control (P < 0.001, Wilcoxon test; reduction in 12 of 13 MCs), while the half duration was not changed (fraction of control 1.02 ± 0.42, P = 0.65). Next, to block $GABA_A$Rs we turned to gabazine (GBZ, 20 µM), since Bicuculline might affect the K^+ channels that contribute to slow AHPs (*Khawaled et al. 1999, Dumenieu et al. 2015*). GBZ alone caused a slightly stronger reduction than APV, which was not significantly different (to 0.71 ± 0.10 of control, n = 7 MCs, P = 0.08 vs APV, not shown). Occlusion experiments using APV before GBZ or GBZ before APV did not result in any further reduction (0.98 ± 0.10 of amplitude in presence of first drug, n = 8 MCs, P = 0.45, Fig. 4F,G). Thus these experiments also support a substantial role of GC NMDARs for GABA release.

From these and the uncaging experiments we conclude that NMDARs located on GCs are strongly involved in reciprocal release, even though prevention of HVACC activation (via Na_v block or pharmacology) also blocks reciprocal release. What is the underlying mechanism? The simplest explanation for a cooperation would be a summation of NMDAR- and HVACC-mediated Ca^{2+} currents at the presynaptic Ca^{2+} sensor. For this scenario two requirements need to be satisfied: (1) temporal overlap of Ca^{2+} currents and (2) spatial proximity of NMDARs and HVACCs within the same microdomain.

Temporal overlap: Simulations of GC spine Ca^{2+} currents via HVACCs and NMDARs

In conventional glutamatergic synapses the NMDAR-mediated postsynaptic current is rising rather slowly compared to the AMPAR-mediated component (rise time ~ 10 ms, *Lester et al. 1990*) and therefore the fractional NMDAR Ca^{2+} current seems at first an unlikely candidate to make direct contributions to fast release. In the reciprocal GC spines however, Na_v channels are locally activated, which enables fast and substantial NMDAR activation. Fig. 5A shows a simulation of the postsynaptic NMDAR- and HVACC-mediated Ca^{2+} currents (based on the detailed NEURON model described in *Aghvami et al. 2019*, see Methods) which illustrates that the local AP causes a transient boosting of the NMDAR Ca^{2+} current because of further relief of the Mg^{2+} block during the upstroke and overshoot of the spine spike. According to the simulation this fast NMDAR-mediated Ca^{2+} spikelet begins even before the HVACC-mediated current and tightly overlaps with it within > 1 ms. Thus HVACC- and NMDAR-mediated Ca^{2+} currents could act in a cooperative manner at the Ca^{2+} sensor(s) that mediate fast release of GABA, especially so, if the release probability was proportional to the fourth power of local $\Delta[Ca^{2+}]$ or more as at other central synapses, and if the channels were close enough to form a microdomain, allowing for an 'overlap bonus' (*Stanley 2016*; Fig. 5B). In the temporal domain, this overlap was found to be highly robust against the variation of the combined Na_v/K_v conductance, and increases in either AMPAR conductance g_{AMPA} or neck resistance R_{neck} resulted in an earlier activation of both HVACC and NMDAR-mediated Ca^{2+} currents and even stronger overlap (Fig. 5C, see Methods). Decreases resulted at first in little change and then a loss of the spine spike whereupon there is no more HVACC activation. To illustrate specifically the contribution of the Na_v-mediated boosting of the NMDAR-mediated Ca^{2+} current, we also calculated the overlap bonus for the HVACC-mediated current as above and the NMDAR current in absence of the spine spike, which indeed renders the cooperative effect negligible (Fig. 5B).

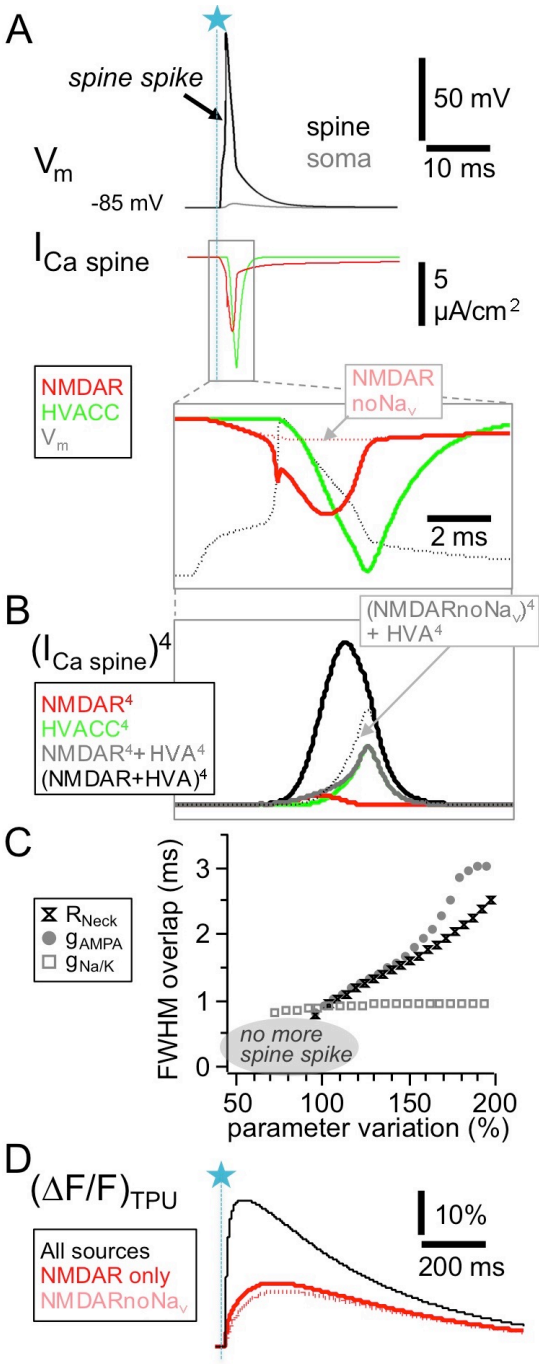

Figure 5. HVACC- and NMDAR-mediated Ca^{2+}-currents overlap temporally in the wake of the spine spike. Simulated spine Ca^{2+}-currents and $(\Delta F/F)_{TPU}$

(**A**) Top panels: spine membrane potential V_m and Ca^{2+}-currents (as in *Aghvami et al. 2019*, their Fig 2B, but without exogenous Ca^{2+} buffer). Bottom: Blow-up of NMDAR- and HVACC-mediated Ca^{2+}-currents, overlaid with the membrane potential V_m. Note the early onset of the NMDAR Ca^{2+}-current and its increase during the underlying local action potential. Red dotted line: NMDAR Ca^{2+}-current in the absence of Na_vs.

(**B**) The temporal coincidence creates an ‚overlap bonus' with respect to local Ca^{2+} concentration and triggering of release: Fourth power of single and added Ca^{2+}-currents. Black dotted line: Addition (hypothetical!) of HVACC with NMDAR Ca^{2+}-current in the absence of Na_vs.

(**C**) Robustness test for extent of overlap between NMDAR- and HVACC-mediated Ca^{2+}-current. Overlap is measured as the stretch of overlapping FWHMs of the current transients (Full Width Half Maxima, see Methods). Parameter variation within 50 - 200% of the nominal value of the neck resistance R_{neck}, the AMPAR conductance gAMPA and the coupled Na_v/K_v conductance $g_{Na/K}$. Results are shown only for parameter runs with spine spike.

(**D**) Simulated fluorescence transients ΔF/F (in the presence of 100 µM OGB-1) show that the contribution of the Na_v-mediated boost of NMDAR Ca^{2+}-currents to the total NMDAR-mediated Ca^{2+} signal is almost negligible (see Discussion).

Spatial proximity: Ultrastructural evidence for presynaptic localization of NMDARs

For fast neurotransmitter release to occur, the current view is that Ca^{2+} entry needs to happen in a proximity of 100 nm or less from the Ca^{2+} sensing part of the SNARE machinery (reviewed in *Kaeser & Regehr 2014; Stanley 2016*). Therefore, to permit cooperation of Ca^{2+} influxes, NMDARs should be localized very close to or within the GABAergic presynapse. Earlier electron microscopic (EM) studies had reported the presence of postsynaptic NMDARs in GC spines and also instances of extrasynaptic labeling (*Sassoè-Pognetto & Ottersen 2000, Sassoè et al. 2003*). To test for the presence of NMDARs near or within GABAergic active zones, we analysed GC spine heads in ultrathin sections that were

immunogold-labeled with either GluN1 or GluN2A/B antibodies (Fig. 6A; see Methods); the sections were selected for the presence of at least one asymmetric (i.e. glutamatergic) contact and/or one symmetric (i.e. GABAergic) contact.

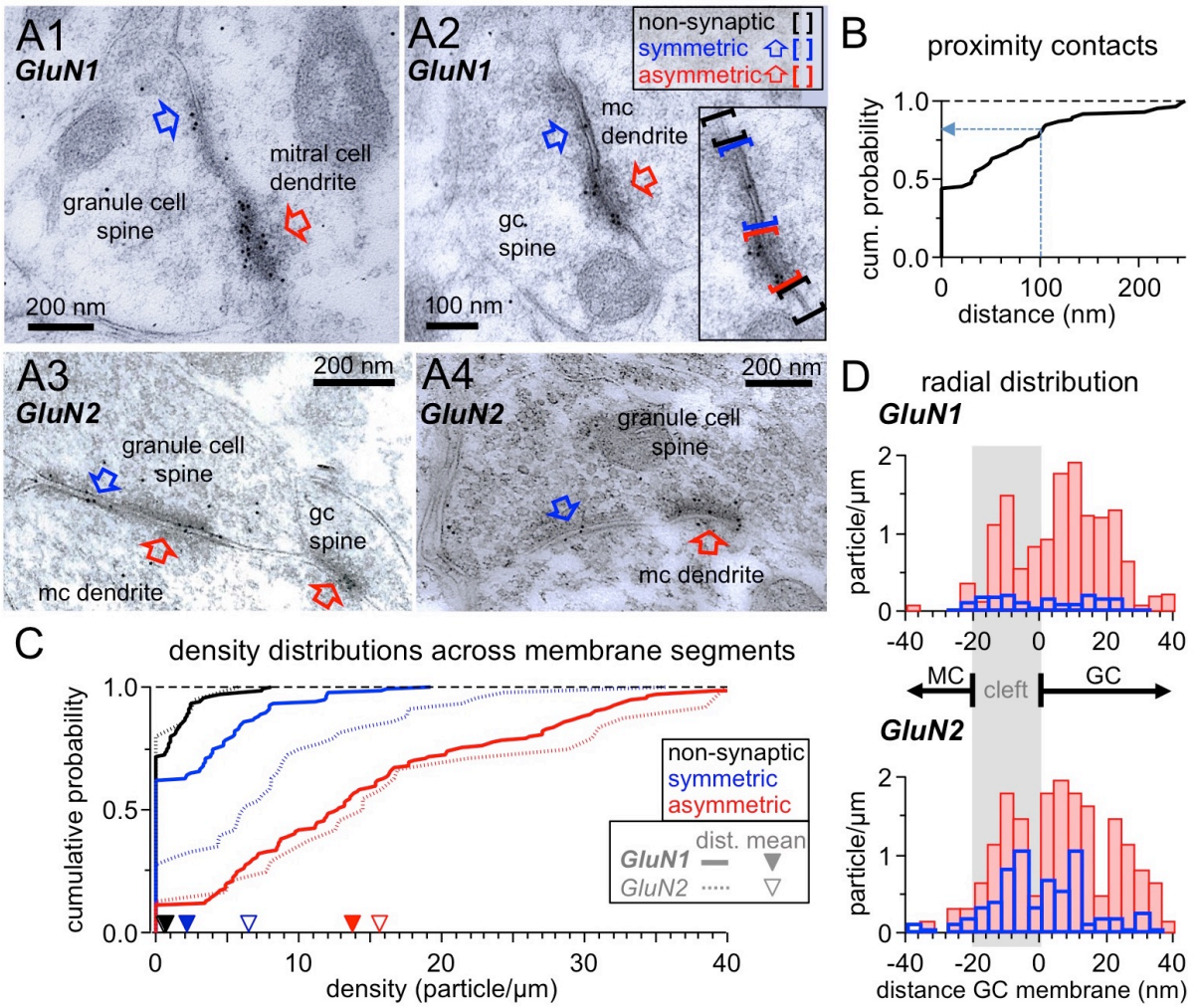

Figure 6. Ultrastructural analysis of the distribution of NMDARs shows their presence at both post- and presynaptic GC spine membranes in reciprocal dendro-dendritic synapses.

(**A**) Representative micrographs of reciprocal dendrodendritic synapses labeled for GluN1 (A1, A2) and GluN2A/B (A3, A4). Note that asymmetric MC-to-GC synapses (red arrows) are strongly labeled and that symmetric GC-to-MC junctions (blue arrows) are also immunopositive. Gold particles are usually not associated with non-synaptic plasma membrane domains of GC spines. The inset in panel A2 illustrates the selection of non-synaptic membrane segments (black brackets), symmetric synapses (blue) and asymmetric synapses (red).

(**B**) Frequency distribution of distances between symmetric and asymmetric synaptic profiles on the same GC spine membrane (based on n = 60 micrographs with both types of profiles on the same spine).

(**C**) Frequency distributions of labeling densities across synaptic (symmetric and asymmetric) and non-synaptic membrane segments for GluN1 (thick lines) and GluN2A/B (thin dotted lines). The arrows on the x-axis indicate the mean density (GluN1: solid, GluN2A/B: open). Color code as in (A).

(**D**) Radial distribution of gold particles representing GluN1 (top panel) and GluN2A/B (bottom panel) at asymmetric (red) and symmetric (blue) synapses. Particle numbers were normalized to the total length of the respective synaptic segments.

Interestingly, we observed that when both symmetric and asymmetric synaptic profiles were visible in individual GC-MC dendrodendritic pairs, the two synaptic profiles were mostly either contiguous (44% of n = 60 cases, examples Fig. 6A2,A3, cumulative plot Fig. 6B) or closer than 100 nm (36% of cases). This finding implies that on both sides of the dendrodendritic synaptic arrangement the postsynaptic specialization very often merges with presynaptic release sites without interposition of non-synaptic membrane domains, and that therefore on the GC side postsynaptic NMDARs can be located very closely to the GABAergic presynapse.

Immunogold labeling for NMDARs was also frequently observed in symmetric contacts, albeit at a lesser density compared to asymmetric contacts (Fig. 6A). To establish whether there is an increased likelihood for the presence of NMDARs at symmetric contacts versus extrasynaptic profiles, we compared the densities of labeling in non-synaptic membrane segments of GC spines with those in symmetric synapses, and as a control in asymmetric synapses. GC spines establishing synapses with MC dendrites were selected as described (see Methods) and all discernible membrane segments within a spine were analysed. For GluN1, there were 50 particles along 84.5 µm of 138 non-synaptic spine membrane segments (mean 0.6 particles/µm), 70 particles along 32.7 µm of 120 symmetric profiles (mean 2.1 particles/µm) and 394 particles along 28.6 µm of 111 asymmetric profiles (mean 13.8 particles/µm). Fig. 6C shows the density distributions across the three types of membrane segments. The distribution of the density of gold particles at symmetric synapses was significantly higher than the one in non-synaptic membrane ($P = 0.000029$, Kolmogorov-Smirnov test). For GluN2A/B, the sample size was smaller, with 5 particles along 10.0 µm of 24 non-synaptic spine membrane segments (mean 0.5 particles/µm), 89 particles along 14.0 µm of 46 symmetric profiles (mean 6.4 particles/µm) and 96 particles along 6.1 µm of 25 asymmetric profiles (mean 15.7 particles/µm). Still, the density distribution at symmetric synapses was significantly higher than the distribution at the non-synaptic membrane ($P = 0.000048$).

Interestingly, while the labeling densities for GluN1 and also GluN2A/B were similar across non-synaptic membranes and asymmetric synapses ($P = 0.99$ and $P = 0.81$, respectively), labeling of symmetric synapses was considerably stronger for GluN2A/B versus GluN1 ($P =$

0.00042). This difference might be due to a distinct receptor configuration and/or a better accessibility of the GluN2 epitopes in the presynaptic symmetric membrane.

Finally, we analysed the radial distribution of particles across synaptic profiles for both antibodies to establish whether labeling was predominantly associated with either the GC or the MC membrane (Fig. 6D; see Methods). The distribution of both GluN1 and GluN2A/B label at asymmetric synapses was similar, with a main peak just inside the postsynaptic GC membrane and another peak within the synaptic cleft. Only a few gold particles were localized beyond 20 nm on the MC side, suggesting that NMDARs are not expressed at significant levels at the glutamate release sites on the MC membrane. Notably, the distribution of gold particles at symmetric synapses mirrored the one at asymmetric synapses, implying that labeling for NMDARs is predominantly associated with both the presynaptic GABAergic and the postsynaptic glutamatergic membrane of GCs.

In summary, we conclude from these findings that NMDARs do play a direct presynaptic role for GABA release from the reciprocal spine, albeit in cooperation with HVACCs (Fig.7). A direct consequence of this conclusion is that any inhibitory output from a GC spine will require the presence of glutamate and thus synaptic input to the respective spine, with far-ranging implications for the role of GC-mediated lateral inhibition in early olfactory processing (see Fig. 8, Fig. 9, Discussion).

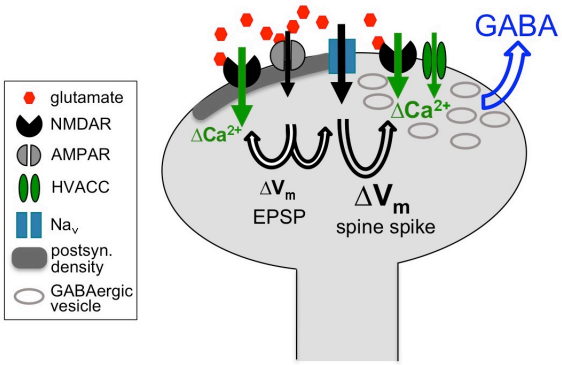

Figure 7 Cooperative release of GABA from the granule cell reciprocal spine
Depolarizing currents are indicated by black solid arrows and Ca^{2+} entry by green solid arrows. Upon binding of glutamate, AMPARs get activated, leading to depolarization of the spine, then activation of both post- and presynaptic NMDARs and Na_vs. The latter in turn drive further depolarization, i.e. the spine spike, which both activates HVACCs and enhances Ca^{2+} entry via NMDARs by additional relief of their Mg^{2+} block. HVACC- and presynaptic NMDAR-mediated Ca^{2+}-currents cooperate to promote release of GABA.

Discussion

Here we have demonstrated that mimicking unitary synaptic inputs via two-photon uncaging of glutamate onto individual olfactory bulb GC spines can activate the entire microcircuit within the spine, from the local spine spike to the release of GABA onto MC lateral dendrites, proving the mini-neuron-like functionality of the reciprocal microcircuit. As in classical axonal release, sequential Na_v channel and HVACC activation triggers output, which occurs on both fast and slow time scales. Strikingly, however, presynaptic NMDA receptors are also found to play a role for GABA release. These findings together with other prior knowledge allow to make an educated guess regarding the specific function of reciprocal spines in bulbar processing (see further below).

Properties of microcircuit operation and implications for coincident local and global activation

For the proximal reciprocal GC inputs investigated here we estimate that under physiological conditions close to the MC resting potential the size of the fast IPSCs is on the order of -5 pA, after corrections for the partial $GABA_AR$ block by DNI and the setting of E_{Cl}. Thus, assuming an *in vivo* MC input resistance of 100 MΩ (*Angelo & Margrie 2011*), an inhibitory input from a single GC spine will exert a somatic hyperpolarization of at best 0.5 mV, and therefore even proximal GC inputs will barely influence MC firing (*Fukunaga et al. 2014; McIntyre & Cleland 2016*) - unless there is coordinated activity across GC spines connected to the same MC dendrite, for example in the wake of an MC action potential during the recurrent IPSP (see e.g. Fig. 4F) or during gamma oscillations (e.g. *Kay 2003; Lagier et al. 2004*).

Upon local activation we observed a GABA release probability P_{r_GABA} from the GC spine on the order of 0.33. This value might represent an upper limit, because the global reduction of inhibition by DNI could cause a homeostatic upregulation of P_{r_GABA} (e.g. *Rannals & Kapur 2011*), and the detection of connections is generally biased towards larger P_{r_GABA}.

With $P_{r\_GABA} \approx 0.3$ and the probability for MC glutamate release on the order of $P_{r\_Glu} \approx 0.5 – 0.75$ (*Egger et al. 2005; Pressler & Strowbridge 2017*) the efficiency of the entire reciprocal microcircuit can be estimated as $P_{reciprocal} = P_{r\_Glu} \cdot P_{r\_GABA} \approx 0.2$, possibly informing future network models. The rather low P_{r_GABA} observed here also implies that GC spines are likely to release with higher probabilities upon coincident global GC signalling (Ca^{2+} spike or global

action potential), due to substantially increased ΔCa^{2+} in the spine (*Egger et al. 2005; Egger 2008; Aghvami et al. 2019; Mueller & Egger 2020)*. We predict this effect to boost both recurrent and lateral inhibition, as described below (Fig. 9).

As to the minimal latency for recurrent GABA release, the temporal resolution of our experiments is limited by the uncaging laser pulse duration (1 ms) and by the unknown exact time course $V_m(t)_{SPINE}$ of the spine spike. Fig. 1E shows that the fastest urIPSCs were detected within 2 ms from TPU onset, implying that there is a fast mechanism coupling Ca^{2+} entry to release - in line with earlier findings of tight coupling between Ca^{2+} entry and GABA release (using EGTA, *Isaacson, 2001*), and of a crucial role for Na_v channels (*Bywalez et al. 2015; Nunes & Kuner 2018*).

While ~ 30% of urIPSCs occurred within 10 ms post TPU onset, there was also a substantial fraction with longer latencies in the range of 10 - 30 ms and some even larger delays. Again, since $V_m(t)_{SPINE}$ is unknown, we cannot determine to what extent these urIPSCs were actually asynchronous (if defined as release events that happen later than the fast coupling of HVA presynaptic Ca^{2+} currents to the release machinery, e.g. *Kaeser & Regehr 2013).* In any case, substantial asynchronous release from the GC spine on yet longer time scales (detected at up to 500 ms post TPU) was frequently observed, in line with earlier studies on recurrent inhibition that localized the origin of asynchronous signalling within GCs (*Schoppa et al. 1998; Chen et al. 2000; Isaacson 2001)*. This time course of asynchronous release also matches with the duration of physiological postsynaptic GC spine Ca^{2+} transients (*Vanessa Lage-Rupprecht & Veronica Egger, unpublished observation*). Thus, the microcircuit can operate across a wide range of latencies, which might contribute to glomerulus-specific GC global AP firing latencies (*Kapoor & Urban 2006*), and also can generate combined synchronous and asynchronous output.

Na_v-mediated and NMDAR-mediated contributions to release

How is postsynaptic Ca^{2+} entry coupled to release of GABA within the GC spine? Previously we have shown via occlusion experiments that Ca^{2+} entry via NMDARs occurs independently from Ca^{2+} entry mediated by the Na_v-HVACC pathway, since AMPAR-mediated depolarization on its own is strong enough to lift the Mg^{2+} block, probably due to boosting by the high GC spine neck resistance *(Bywalez et al. 2015)*. Therefore, we initially hypothesized

that the Na_v-HVACC pathway would provide the sole trigger for fast release of GABA, as in classical release from axons (see also *Nunes & Kuner 2018*), reinforcing the notion of the GC spine as an independent mini-neuron that can generate output via its own local AP. Indeed, blockade of either Na_v or HVACCs strongly reduced or abolished urIPSCs. However, in subsequent experiments probing NMDAR contribution we observed that urIPSCs were also massively reduced by blockade of NMDARs.

As a note of caution, activation of single GC spines via TPU might involve spurious activation of extrasynaptic NMDARs. We had observed that TPU resulted in a slightly larger NMDA-receptor mediated component of the postsynaptic Ca^{2+} signal than true synaptic activation via glomerular stimulation (~ 65 % vs ~ 50% of $\Delta F/F$, *Bywalez et al. 2015; Egger et al. 2005*). Thus, at least part of the strong impact of NMDARs observed here might have been rooted in their over-activation. Therefore, we investigated recurrent inhibition elicited by single MC APs, and could demonstrate that NMDAR blockade alone (which does not prevent GC spine spike generation, *Bywalez et al. 2015*) also reduces recurrent inhibition. This effect was found to be mutually occlusive with the effect of $GABA_AR$ blockade, arguing again in favor of an essential role of NMDARs for GABA release and against systematic overstimulation in the TPU experiments (see also Results, Methods).

Another interesting aspect of the strong influence of NMDARs on GC output is that this property might serve to differentiate the MC↔GC microcircuit from the MC↔PV+ cell microcircuit, since PV+ cells feature Ca^{2+}-permeable AMPARs and a probably absent NMDAR component in response to MTC input (*Kato et al. 2013*). Thus, the urIPSC blockade by APV observed here further argues in favor of a preferential activation of the MC↔GC circuit by our experimental method.

In our previous study of postsynaptic Ca^{2+} signals in GC spines there was no obvious influence of Na_v activation on NMDAR-mediated Ca^{2+} entry (*Bywalez et al. 2015*). At first, this finding might seem at variance with the simulations in Fig. 5 that demonstrate a boosting of early NMDAR-mediated Ca^{2+} currents by the spine spike. However, the simulations also indicate that this extra contribution is not substantial in terms of added $\Delta F/F$ under our experimental conditions and therefore could not be detected (Fig. 5D). In line with the fast NMDAR-mediated Ca^{2+} spikelet, *Kampa et al. (2004*) have shown that the earlier the

postsynaptic membrane is depolarized after glutamate release, the more efficiently NMDARs will be activated. These observations are of general importance in the context of spike-timing dependent plasticity and electrical compartmentalization of spines (e.g. *Grunditz & Oertner 2004, Tonnesen & Nägerl 2016*).

How exactly do NMDARs now effect release? The Na_v/NMDAR-mediated Ca^{2+} spikelet results in substantial and fast coincident activation of NMDARs and HVACCs, and our ultrastructural evidence for presynaptic NMDARs implies that indeed these currents can feed into the same presynaptic microdomain (see Results). This overlap bonus at the presynaptic Ca^{2+} sensor (as predicted by the simulations) is likely to underlie the observed cooperative signalling of HVACCs and NMDARs.

Direct involvement of presynaptic NMDARs in GABA release

Presynaptic actions of NMDARs at specific subsets of both glutamatergic and GABAergic synapses have recently received attention (reviewed *in Bouvier et al. 2015; Banerjee & Paulsen 2016*). Presynaptic NMDARs have been shown to play a role in plasticity induction (e.g. *Duguid & Smart 2004*) or in modulation of basal synaptic transmission, where effects are mostly observed upon repetitive transmitter release (e.g. *McGuiness et al. 2010*). Presynaptic NMDARs in the cerebellum are also involved in enhancing spontaneous release of GABA (*Glitsch & Marty 1999*), with similar recent observations for extrasynaptic NMDA receptors on retinal A17 amacrine cells (V*eruki et al. 2019*). However, to our knowledge direct triggering of release via presynaptic NMDARs during unitary transmission has not been observed so far, adding another pathway to the already highly diverse signalling downstream of NMDARs.

The observed cooperation between Na_v/HVACCs and NMDARs relates our study back to the initial studies on dendrodendritic recurrent inhibition (DDI), when it was concluded by several groups that NMDARs can contribute directly to release from the reciprocal spine upon extended release of glutamate from the MC dendrite (see Introduction), and *Schoppa et al. (1998*) already speculated that this presynaptic function might be related to either Ca^{2+} entry or depolarization. However, the relative contribution of NMDARs has been under debate and it was demonstrated that under physiological conditions HVACC activation would be the dominant release trigger (*Isaacson 2001*). While the standard DDI protocol, using 20-50 ms

long depolarizations, would evoke recurrent inhibition also in the presence of TTX (possibly even enhanced, *Halabisky et al. 2000*), it was reported that recurrent inhibition in response to shorter steps (< 5 ms) is substantially smaller than for the long step and reduced in TTX (*Schoppa et al. 1998; Halabisky et al. 2000*). In view of our above findings, the standard DDI protocol is likely to recruit NMDAR-dependent pathways for triggering GABA release via prolonged release of glutamate and subsequent summation of EPSPs in GC spines, whereas short steps are more likely to trigger release via the GC spine spike. Thus, the cooperation of NMDARs and HVACCs reconciles these earlier findings.

Reciprocal inhibition and spontaneous inhibitory activity

Spontaneous IPSCs are likely to predominantly originate from the more proximal lateral MC dendrites (*Arnson & Strowbridge 2017*). The slightly larger mean amplitude of sIPSCs compared to the triggered urIPSCs observed here might be explained by perisomatic inhibitory contacts onto MCs, e.g. from type S GCs (*Naritsuka et al. 2009*). All three antagonists of urIPSC generation (TTX, CTX, APV) were found to also substantially reduce sIPSC frequency. For Na_v blockade, strong effects on MC sIPSCs were reported also elsewhere (e.g. *Halabisky et al. 2000; Arnson & Strowbridge 2017*) and are expected because of the blockade of spontaneous MC firing and the GC spine spike. The effect of HVACC blockade was less pronounced than that of Na_vs, probably because it will not prevent spontaneous MC firing.

The substantial effect of NMDAR blockade on spontaneous IPSCs was also observed in other olfactory bulb studies (*Wellis & Kauer 1993; Schmidt & Strowbridge 2014; but see Chen et al. 2000*). Several factors might contribute: (1) the long-lasting depolarizations in MCs that are enhanced by NMDAR activation (*Carlson et al. 2000*), (2) the presence of MC NMDA autoreceptors (*Sassoé-Pognetto et al. 2003*), and (3) the crucial role of NMDARs for release from the GC spine reported here, since spontaneous release of glutamate from MCs is unlikely to trigger recurrent IPSCs in the presence of APV.

Functional role of presynaptic NMDARs in GC spines: Linking coactive glomerular columns

While a presynaptic contribution of NMDARs to GABA release from GCs was already demonstrated earlier (see above), our findings imply that not only **can NMDAR activation**

trigger GABA release, it is actually necessary, also in the presence of a Na_v-mediated spine spike. This observation is very intriguing for several reasons:

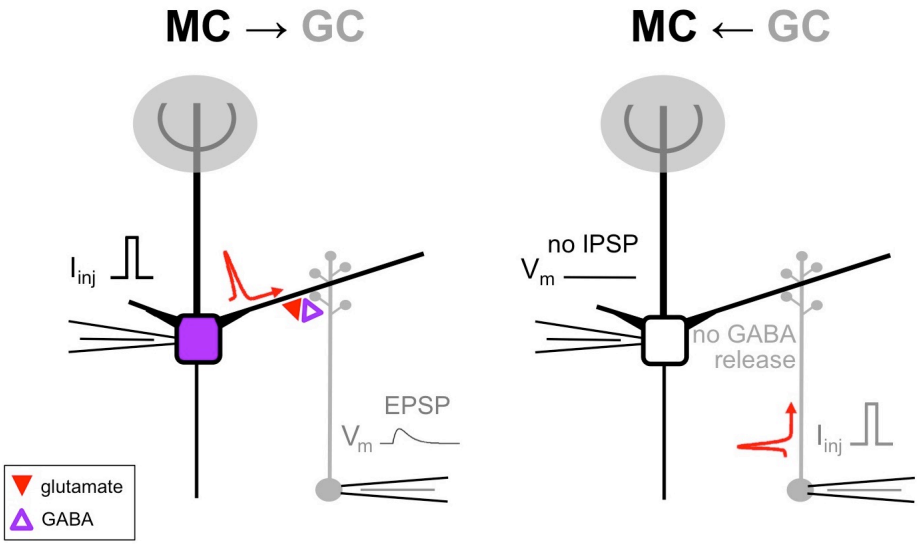

Figure 8. Action potentials alone are unlikely to cause release from GCs, thus no apparent reciprocal connectivity is oberved in coupled GC↔MC pairs.
Left: Recording situation for connection MC→GC. A MC action potential is elicited by somatic current injection and propagates along the lateral dendrite. An EPSP will be detected at the GC soma. Recurrent release of GABA will be triggered at the reciprocal synapse (see also Fig. 7).
Right: Recording situation for connection GC→MC. A GC action potential is elicited by somatic current injection and propagates into the apical dendrite and its spines. However, this action potential will not trigger release of GABA, since there is no glutamate present at the reciprocal synapse to activate the presynaptic NMDARs, and hence no IPSP will be recorded at the MC soma.

(1) No AP-mediated release from the reciprocal spine without synaptic input.

Notwithstanding the precise site of AP generation in GCs, any AP will propagate along the GC dendrite and the reciprocal spines perfectly well (*Egger et al. 2003, Pressler & Strowbridge 2019*). The ensuing spine depolarization $V_m(t)_{SPINE}$ will resemble that of the spine spike (*see also Aghvami et al. 2019*) which on its own, with NMDARs blocked, according to our findings cannot trigger GABA release. Therefore, any action potential that propagates within the GC is rather unlikely to cause release of GABA by itself. This consequence explains why no reciprocal connectivity was reported from paired recordings of MCs coupled to GCs so far (*Isaacson 2001, Kato et al 2013, Pressler & Strowbridge 2017*) and why others including our group have been unable to find connected GC → MC pairs in paired recordings in the first place (see *Egger et al. 2003, Schoppa 2006*), since functional connectivity is tested by eliciting APs in the putative presynaptic cell (see Fig. 8). This lacking proof of functional connectivity has been

particularly enigmatic in view of plenty of ultrastructural evidence that spines between MCs and GCs are usually reciprocal (e.g. *Price & Powell 1970, Jackowski et al. 1978, Woolf et al. 1991*), and of the strong physiological evidence for GC-mediated recurrent inhibition of MCs. It should be noted that extracellular stimulation of the GC layer can elicit MC inhibition, even in the presence of APV (*e.g. Chen et al 2000, Egger et al. 2003, Arevian et al. 2008*). Possible explanations might be that either there is still some small remaining probability for GABA release from spiking GCs in the absence of glutamate, or that this type of stimulation activates some as of yet unknown inhibitory input to MCs, e.g. via deep short-axon cells or axons of EPL interneurons (*Nagayama et al. 2014, Burton 2017*).

(2) Role of GC-mediated lateral inhibition between MCs.

It is known by now that broad, far-range lateral inhibition between mitral cells within the EPL is mediated by other interneurons than GCs (see Introduction). Thus, GCs are unlikely to dominate bulbar lateral inhibition in terms of magnitude, i.e. total charge transfer, a view that is also supported by other recent studies (*Fukunaga et al. 2014, Geramita & Urban 2017*). What then is the function of GC-mediated lateral inhibition?

Activation of a given olfactory receptor will in turn activate its associated glomerular unit and the neurons belonging to the respective glomerular column. In the following, a given GC belongs a glomerular column if it can be fired (globally or regionally) via the activation of the MTCs associated with that column. Evidence for GC spiking upon uniglomerular activation *in vitro* has been observed by several groups, including our own (e.g. *Schoppa et al. 1998, Egger 2008, Stroh et al. 2012; Burton & Urban 2015*); moreover, we have shown recently that rather low numbers of coactivated spines on GC apical dendrites (< 10) are sufficient to elicit dendritic spiking (*Mueller & Egger, 2020*).

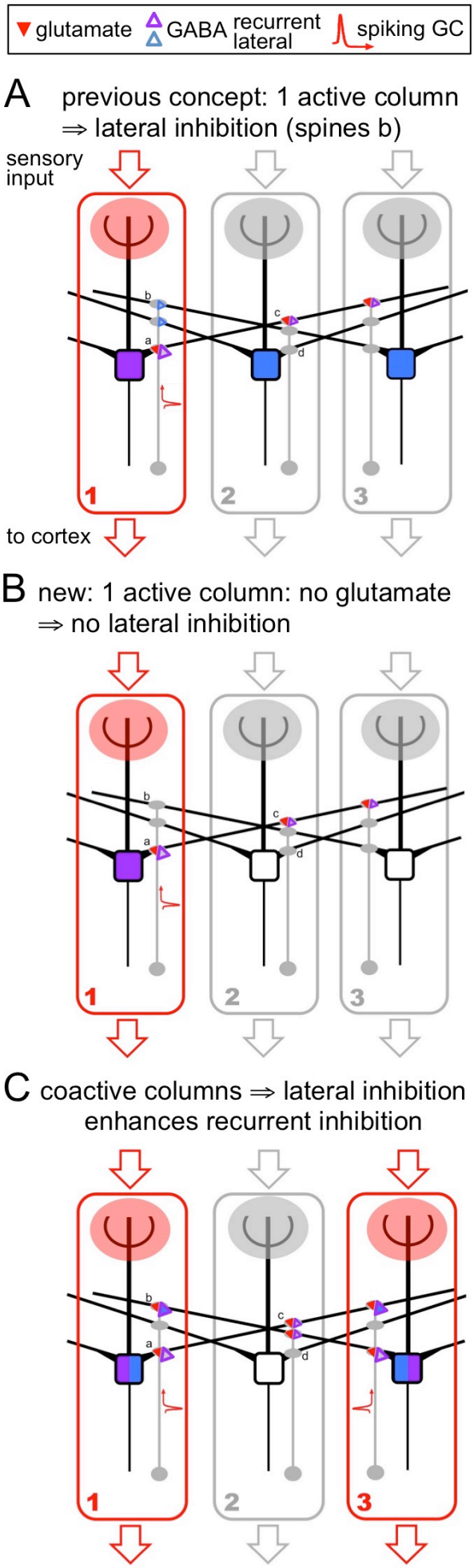

Figure 9 GC-mediated lateral inhibition: previous and new concept

In each schematic column, the depicted mitral cell and granule cell stand for the ensemble of all MCs and GCs belonging to the column. GCs belong to a column if they can be fired (globally or regionally) by the ensemble of active columnar MCs (and thus a given GC may belong to more than one column). All three columns are interconnected via MC-GC-MC interactions. There are four GC spine types: a: spines receiving MC input within the column, b: other spines that belong to GCs within the column but without columnar input, c: spines in other columns that are laterally connected to the active column, d: spines in other columns that are not laterally connected to the active column.

A Classical hypothesis

Column 1 gets activated by sensory input. Its MCs fire and receive recurrent inhibition from the GC spines they are connected to, both from within the column (spines a) and from others (e.g. spines c). Upon firing of the columnar GCs, these release GABA from their reciprocal spines, including contacts to other columns (spines b). Note that the columnar outputs (spines a) will exert stronger recurrent inhibition than the non-columnar spines c because of the coincidence of the GC spike with the local input. Thus recurrent inhibition at spines a will be enhanced. The MCs in column 1 will receive recurrent inhibition and the MCs in the other columns 2,3 will receive lateral inhbition.

B New hypothesis, scenario I: One active column.

If only one column is activated, lateral inhibition will not happen since spines b do not receive any glutamate and the propagating spike alone is not sufficient for GABA release (see also Fig. 8). Still, there will be recurrent inhibition from spines c. Note that the enhanced recurrent inhibition at spine a will also happen in this scenario.

C New hypothesis, scenario II: Coactive columns.

If two or more columns are coactive, again there will be enhanced recurrent inhibition at their spines a. In addition, spines b in column 1 will now exert recurrent inhibition of the coactive column 3 and this recurrent inhibition will be enhanced by the coincidence of the GC spike in column 1 with the lateral input, thus lateral inhibition will also be exerted. If the connectivity and the strength of activation are symmetric, the situation in column 3 is symmetric, resulting in mutual lateral inhibition and thus possibly synchronized output.

Thus the MCs within the active columns 1, 3 will receive recurrent inhibition enhanced by lateral inhibition and the MCs in the silent column 2 will not be inhibited at all. Even if the GCs in column 2 would become fired by multiple coincident lateral inputs, they will not release GABA on the MCs of column 2, since again there is no glutamate at the respective contacts.

614

Figure 9A illustrates the prevailing concept of GC-mediated lateral inhibition up to now. Upon spiking (global or regional) the spikes will result in GABA release not only at the reciprocal synapses that have received input from an active glomerulus but also in GABA release from other spines invaded by the spike that connect to extra-glomerular mitral cells, exerting lateral inhibition. The spatial structure of this lateral inhibition depends on anatomical connectivity and network dynamics and has been proposed to be either isotropic, consistent with a center-surround field as in the retina, or rather patchy (reviewed in *Murthy 2011*; see also *Chae et al. 2019*). Note however, that most of the involved studies did not investigate specifically GC-mediated lateral inhibition.

In any case, the columnar GC spines (i.e. those that receive synaptic input from the active column) will experience coincident local spine spikes and global spikes, resulting in enhanced local Ca^{2+} entry, and therewith are likely to increase their release probability P_{r_GABA} (see above).

However, as a consequence of the requirement of presynaptic NMDAR activation, there will be no or at best very little GC-mediated lateral inhibition upon activation of a single column (Fig. 9B). We predict that GC-mediated **lateral inhibition will happen predominantly across coactive columns**, such that a local synaptic input originating from a lateral active column will coincide with a global (or regional) columnar spike, resulting in enhanced inhibition of the lateral coactive column. The mechanism is the same as for the coincidence detection described above for recurrent inhibition within an active column (Fig. 9C). Provided that there are mutually interconnecting GCs in both columns, this effect will be symmetric.

Therefore, GC-mediated lateral inhibition acts non-topographically (i.e. not isotropically) to enhance recurrent inhibition. Non-topographical lateral interactions in the bulb have been proposed already previously based on functional evidence and simulations (e.g. *Urban & Arevian 2009, Shepherd et al. 2007, Fantana & Meister 2008*). While non-topographic lateral inhibition may also happen within the glomerular layer (e.g. *Cleland & Sethupathy 2006, Economo et al. 2016*), our hypothesis is built on the spine-specificity of GABA release. It does not require a specific, pre-established anatomical connectivity but

is a property of the synaptic arrangement of the microcircuits. Connectivity is dynamically restricted to coactive columns and thus matched to glomerular activation patterns.

This mechanism will allow GC-mediated lateral inhibition to participate in synthesizing the olfactory percept at the level of the bulb from the individual olfactory receptor channels, most likely via synchronization in the gamma band (e.g. *Laurent et al. 1996, Kashiwadani et al. 1999, Schoppa 2006, Brea et al 2009, Li et al. 2015, Peace et al. 2017*), while at the same time preventing unnecessary energy expenditure and unwanted inhibition of other glomerular columns (i.e. if GABA release would happen from all spines of an activated GC). Thus inactive columns will remain sensitive for new stimuli or changing components because they are not inhibited.

In other words, the discovered mechanism allows GCs to perform **lateral inhibition "on demand",** selectively on co-active mitral cells, and **thus can provide directed, dynamically switched lateral inhibition in a sensory system with 1000 receptor channels, therefore explaining the unusual microcircuit of the GC spine/mini-neuron as a means of olfactory combinatorial coding.**

Previous evidence for activity-dependence of lateral inhibition and impact of NMDARs

There is substantial prior evidence in the literature for both the activity-dependence and NMDAR-dependence of GC-mediated lateral inhibition. Activity-dependent lateral inhibition was already observed *in vitro* between pairs of MCs; one 'sending' cell was made to fire at a high frequency, whereas the other 'receiving' cell was either not activated at all or subjected to evoked spike trains with increasing frequency (*Arevian et al., 2008*). The receiving MC showed effects of lateral inhibition by the sending MC within a certain range of its own firing, but never for low or no own firing. The authors argue that the activity-dependent effect is due to increased recruitment of firing of interconnecting GCs with increased activity (due to the summation of inputs from both sending and receiving MCs); while such summation can certainly contribute, our results further clarify the reason for a complete lack of lateral inhibition of silent MCs.

Yet more importantly, in *in vivo* recordings from MCs there was a subset of MCs that responded exclusively with inhibition to odor activation, presumably via lateral inhibition (*Fukunaga et al., 2014, their Fig 4 and 7)*. However, optogenetic silencing specifically of GCs

had no effect whatsoever on this lateral inhibition both in anesthetized and in awake animals, whereas silencing of glomerular inhibitory neurons did. Our results can explain this lack of contribution of GCs to lateral inhibition by the lack of odor-evoked activity in the recorded MCs – thus the presynaptic NMDARs could not be activated and no GC output would occur.

A third line of evidence is provided by the fact that markers of neuronal activity (such as c-Fos or 2-deoxyglucose) have revealed the existence of glomerular units/columns spanning all layers of the bulb (e.g. *Kauer & Cinelli 1993*). More recently, retrograde transsynaptic tracing studies using pseudorabies virus injections in the olfactory bulb and piriform cortex have further confirmed this concept, by labeling of subsets of glomerular columns dispersed across the bulb, which very frequently contained a substantial fraction of GCs (*Willhite et al. 2006, Kim et al. 2011*). The authors already speculated that this patchy labeling could be explained by activity-dependent transsynaptic crossing from MC lateral dendrites, i.e. specifically to active GC spines, which matches with the powered release of GABA restricted to activated columns predicted by our results. Indeed, a recent study has been able to produce compelling evidence for activity-dependent retrograde transsynaptic viral spread (albeit by rabies virus, not pseudorabies; *Beier et al. 2017*). We would predict that interference with GC-NMDAR signalling should prevent the transsynaptic labeling of GCs.

Interestingly, *McTavish et al. (2012*) have demonstrated in simulations that columnar arrays of GCs may be particularly effective in mediating synchronization, if the lateral connectivity is symmetric, in line with our hypothesis. To further elucidate this possibility, it would be important to know the impact of more distal GC inputs that were not investigated here for technical reasons. *In vivo*, distal excitation of GCs and accordingly large MC receptive fields have been demonstrated using optical stimulation (*Peace et al. 2017*).

As to functional evidence for a strong role of NMDARs in GC-mediated lateral inhibition, NMDAR blockade is routinely used to dissect lateral inhibition in the glomerular layer from GC-mediated lateral inhibition *(Shao et al. 2012, Najac et al. 2015, Geramita & Urban 2017)*. NMDARs play a crucial role in enabling supralinear dendritic integration in GCs, efficiently lowering the threshold for global spiking and thus also for lateral inhibition (*Mueller & Egger 2020*). Both GC NMDARs and Na_vs are known to play a role specifically in discriminations between binary odorant mixtures in mice, since in the same behavioral paradigm GC-specific

704 knock-down (in about ~ 50% of GCs) of the NMDAR-subunit GluN1 resulted in an increase in
705 discrimination time of on average ~ 60 ms, and knock-down of Na_vs of ~ 85 ms versus
706 control, while discriminations between pure odors were not affected (*Abraham et al., 2010;*
707 *Nunes & Kuner 2018*). These similar effects are in line with our findings, since both
708 modifications should prevent both recurrent and lateral inhibition. However, the relative
709 impact of recurrent inhibition versus lateral inhibition is not known.
710 Moreover, while there is first evidence for substantial dendritic Ca^{2+} signals and local GC
711 spine signals *in vivo* (*Wienisch & Murthy 2016; Wallace et al. 2017; Zhang et al. 2016*), the
712 extent to which specifically local GABA release from GC spines contributes to odor
713 processing in the olfactory bulb is difficult to estimate at this point. Future methodological
714 advances will be required to tackle the contribution of the GC spine spike along with its
715 cooperative release mechanism to bulbar processing, including voltage-sensitive dye
716 imaging and novel genetic loss-of-function approaches for dissecting local recurrent release
717 from lateral inhibition - perhaps by targeting specifically presynaptic NMDARs.
718 *Conclusion: The purpose of the reciprocal spine*
719 In summary, we suggest that reciprocal spines allow the granule cell to selectively interact
720 with coactive glomerular columns. Thus, the reciprocal spine might be a circuit motif that
721 specifically enables efficient binding of dispersed olfactory representations, a coding task that
722 this sensory modality needs to perform due to its large number of receptors. In other words,
723 reciprocal spines with their unique synaptic arrangement and functionality, including spine
724 spikes and presynaptic NMDARs, represent a special adaptation to the demands of sensory
725 processing in the bulb.
726 Another intriguing yet more speculative potential function of target-activity-dependent output
727 is that concurrent preactivation from glutamatergic cortical inputs onto reciprocal spines
728 (ultrastructure in *Price & Powell 1970*) can also enable or enhance lateral inhibition (in
729 addition to providing feed-forward inhibition), allowing for a top-down projection of olfactory
730 templates as has been proposed by *Zelano et al. (2011*).
731

Methods

Animal handling, slice preparation and electrophysiology

Animals used in our experiments were juvenile Wistar or VGAT-Venus transgenic rats (VGAT-Venus /w-Tg(SLc32a1-YFP*)1Yyan) of either sex (P11 – P19). VGAT-Venus transgenic rats are based on mouse BAC transgenic lines. They were generated by Drs. Y. Yanagawa, M. Hirabayashi and Y. Kawaguchi at the National Institute for Physiological Sciences, Okazaki, Japan, using pCS2-Venus provided by Dr. A. Miyawaki (*Uematsu et al., 2008*), RRID: RGD_2314361. In this rat line, fluorescent Venus protein is preferentially expressed in cells carrying the vesicular GABA transporter (VGAT), i.e. GABAergic neurons: the localization of Venus-labeled cells across OB layers was found to be similar to that of GABA-positive cells; direct colocalization in the cortex yielded an overlap of 97% (*Uematsu et al., 2008*).

Sagittal olfactory bulb brain slices (thickness 300 µm) were prepared in ACSF (composition see below) following procedures in accordance with the rules laid down by the EC Council Directive (86/89/ECC) and German animal welfare legislation. Slices were incubated a water bath at 33°C for 30 min and then kept at room temperature (22°C) until recordings were performed.

Olfactory bulb mitral cells were visualized by gradient contrast and recorded from in whole cell voltage clamp mode (at -70 mV or +10 mV) or current clamp mode. Recordings were made with an EPC-10 amplifier and Patchmaster v2.60 software (both HEKA Elektronik, Lambrecht/Pfalz, Germany). Experiments were performed at room temperature (22°C). Patch pipette resistance ranged from 5-6-MΩ. Mitral cells clamped at -70 mV were filled with intracellular solution containing the following substances (in mM): (1) tip solution: 130 K-Methylsulfate, 10 HEPES, 4 MgCl2, 2 Ascorbic acid, 10 Phosphocreatine-di-tris-salt, 2.5 Na2ATP, 0.4 NaGTP (2) backfilling solution: 110 Cs-Chloride, 10 HEPES, 10 TEA, 4MgCl2, 2 Ascorbic acid, 10 5-N-(2,6-dimethylphenylcarbamoylmethyl) triethylammonium bromide (QX-314, Sigma), 0.2 EGTA, 10 Phosphocreatine, 2.5 Na2ATP, 0.4 NaGTP. Mitral cells clamped at + 10 mV contained internal solution composed of: 125 Cs-methanesulfonate 1 NaCl, 0.5 EGTA, 10 HEPES, 3 MgATP, 0.3 NaGTP, 10 Phosphocreatine-di-Tris-salt, 10 QX-

314, 0.05 Alexa 594 (Ca^{2+} indicator, Thermofisher Scientific, Waltham. Massachusetts, US), at pH 7.3.

For current clamp experiments the internal solution contained: 130 K-Methylsulfate, 10 HEPES, 4 MgCl2, 2 Ascorbic acid, 10 Phosphocreatine-di-Tris-salt, 2.5 Na2ATP, 0.4 NaGTP. Single APs were evoked by somatic current injection (3 ms, 1 nA) and 5 APs were elicited for every recording condition. Cells with leak currents > 200 pA (at V_{hold} = - 70 mV) were discarded. We chose a hyperpolarized holding potential in order to reduce the activation of NMDA autoreceptors on MC lateral dendrites.

The extracellular ACSF was bubbled with carbogen and contained (in mM): 125 NaCl, 26 $NaHCO_3$, 1.25 NaH_2PO_4, 20 glucose, 2.5 KCl, 1 $MgCl_2$, and 2 $CaCl_2$. The following pharmacological agents were bath-applied in some experiments: bicucculline (BCC, 50 µM, Sigma-Aldrich), ω-conotoxin MVIIC (CTX, 1 µM, Alomone, Jerusalem, Israel), TTX (500 nM, Alomone), D-APV (25 µM, Tocris), gabazine (GBZ, 20 µM, Tocris). In pharmacological experiments we waited for 10 minutes after wash-in of the drugs TTX, APV resp. CTX. In CTX experiments 1mg/ml cyctochrome C was added to the ACSF. TTX voltage clamp experiments were conducted at clamping potentials of -70 mV (n = 5) or + 10 mV (n = 7), whereas all CTX and APV voltage clamp experiments were conducted at + 10 mV.

Combined two-photon imaging and uncaging

Imaging and uncaging were performed on a Femto-2D-uncage microscope (Femtonics, Budapest, Hungary). Two tunable, Verdi-pumped Ti:Sa lasers (Chameleon Ultra I and II respectively, Coherent, Santa Clara, CA, USA) were used in parallel. The first laser was set either to 900 nm for simultaneous excitation of YFP and Alexa 594 in one channel for visualization of spines and the mitral cell for urIPSC recordings, and the second laser was set to 750 nm for uncaging of caged glutamate. The two laser lines were directly coupled into the pathway of the microscope with a polarization cube (PBS102, Thorlabs Inc, Newton, NJ, USA) and two motorized mirrors. As caged compound we used DNI-caged glutamate (DNI; Femtonics). DNI was used in 1 mM concentration in a closed perfusion circuit with a total volume of 12 ml. Caged compounds were washed in for at least 10 minutes before starting measurements. The uncaging laser was switched using an electro-optical modulator

(Pockels cell model 350-80, Conoptics, Danbury, CT, USA). The emitted fluorescence was split into a red and a green channel with a dichroic mirror.

Triggering of mitral cell reciprocal IPSCs

The region of interest on a proximal lateral mitral cell dendrite was moved to the center of the scanning field. In some initial experiments, four uncaging spots were placed in close apposition along the lateral mitral cell dendrite in case of 'blind' uncaging (n = 8 out of total number of successful experiments n = 44). In most experiments, a single uncaging spot was positioned near the region of interest, using YFP fluorescence of GABAergic cells in VGAT-Venus rats as an optical guide to identify potential synaptic contacts between MC lateral dendrites and GC spines.

The parameter settings for two-photon uncaging were as established previously on the same experimental rig for precise mimicking of unitary synaptic Ca^{2+} transients in GC spines (*Egger et al. 2005; Bywalez et al. 2015*). These parameter settings were routinely verified in parallel test experiments, where we imaged Ca^{2+} transients in GC spines following TPU (as in *Bywalez et al. 2015)*. The uncaging site was usually chosen within the top 10-30 µm below the slice surface (since otherwise the visibility of spines in the Venus-VGAT rats was compromised) and the uncaging power was adjusted to the depth of the uncaging site, corresponding to a laser power of approximately 15 mW at the uncaging site (*Sobczyk et al. 2005*). The uncaging beam was positioned at ~ 0.2 - 0.5 µm distance from the MC dendrite/GC spine head. The uncaging pulse duration was 1 ms. The scanning position was readjusted if necessary before each measurement to account for drift. The microscope was equipped with a 60x Nikon Fluor water immersion objective (NA 1.0; Nikon Instruments, Tokyo, Japan). The microscope was controlled by MES v.5.3190 software (Femtonics). To prevent overstimulation, the uncaging laser power was **not** increased if there was no detectable response. While we cannot exclude overstimulation per se, we would like to argue that systematic overstimulation is unlikely to have occurred based on the following observations (see also Results):

- size of urIPSCs as compared to spontaneous activity (Fig. 1F)
- low reciprocal release probability from the spine (Fig. 1F)

- no extended asynchronous release compared to the classical experiments on recurrent inhibition (mean total duration of TPU-evoked recurrent inhibition ~ 200 ms, Fig. S1E, vs a mean half duration ~ 500 ms in e.g. *Schoppa et al. 1998, Isaacson 2001*)
- no evidence for toxicity in our stability experiments (Fig. 1E)
- main finding of dependency of recurrent inhibition on NMDAR activation confirmed by method that does not involve uncaging

Uncaging stability

To test for the stability of uncaging evoked recurrent IPSCs in MCs, uncaging at a dendritic region of interest was performed. If repeated uncaging led to the apparent occurrence of urIPSCs within the same time window (see below for anlysis details), the stability measurement was continued by either uncaging 30 times in total with a frequency of 0.033 Hz (every 30 s) or 5 times in a row with 0.033 Hz followed by a 10 min break (to mimic the time for wash-in of pharmacological compounds) and another round of uncaging (5x, 0.033Hz). urIPSC amplitudes were taken from averages of the first 5 – 10 and the last 5 – 10 uncaging sweeps and statistically compared with each other.

Electrophysiology: Data analysis and statistics

Electrophysiological data were analysed with custom written macros in Igor pro (Wavemetrics, Lake Oswego, OR, USA). Additional sIPSC and urIPSC analysis was performed using the MiniAnalysis program (Synaptosoft, Decature, GA, USA) and Origin (Northampton, MA, USA).

Detection of urISPCs Due to the high spontaneous activity, in order to test for the presence of a signal we performed first an area and event analysis of IPSC traces (see below and Fig. 1D; if a signal was detected based on these analyses, we went on to search for individual triggered urIPSCs by visual inspection of an overlay of the recorded traces. Individual IPSCs were considered as uncaging-evoked when they repetitively occurred within the same time window (width 3 ± 2 ms, n = 35) after uncaging and had similar kinetics (indicating a similar location of the respective input on the dendrite). Signal types ranged from single urIPSC

events to barrages of urIPSCs lasting tens to hundreds of ms. The release probability was estimated based on 5 – 30 TPU samplings with a mean of 7.5 ± 1.7 stimulations (n = 44).

Area analysis The area was measured in individual traces as the integrated activity above baseline for a 500 ms pre-uncaging baseline window and for a 500 ms post-uncaging window, in order to screen for the presence of a signal (Fig. 1D). The 500 ms extent of the time windows was validated by our measurements of averaged barrage duration (see Fig. S1D2).

Delta (Δ) area values were calculated by subtracting the area of the 500 ms pre-uncaging baseline window ('pre') from the 500 ms post-uncaging window ('post'), in order to isolate the amount of uncaging-evoked inhibitory activity from spontaneous activity. If this procedure was applied to averaged traces and the result was negative, the Δ_area value was set to zero (i.e. no uncaging-evoked activity). While this procedure might still generate false positives due to spontaneous bursts of activity in the post-uncaging window, it also prevents a spurious cancelling of activity (false negative) that otherwise might happen upon averaging Δ_area across an entire set of experiments. Δ_area values for pharmacological conditions were normalized to control Δ_area in order to assess the net effect of drugs on uncaging-evoked inhibitory activity (Fig. 2D, 3D, 4D).

Event analysis Within the individual recorded traces, the peak time points of individual IPSCs were analysed. Peak search parameters in MiniAnalysis were adjusted in order to detect potentially all IPSCs within a trace. For detailed spontaneous IPSC amplitude analysis, IPSCs were sorted manually after the automated peak search and discarded if the amplitude exceeded less than 5 pA and/or the IPSC onset was not be detected properly. Event counts were averaged for the 500 ms pre-uncaging and the 500 ms post-uncaging windows, respectively.

Evaluation of effects of pharmacological agents For determining drug effects, the averaged urIPSC amplitudes were scaled down by the ratio of number of responses to total number of trials, both in control and drug condition, in order to account also for changes in release probability. If no single responses/urIPSCs could be detected anymore in the presence of TTX, CTX or APV according to the criteria described above, we measured the mean amplitude of V_m above baseline in the averaged response at the time point of the maximal

response amplitude in control condition. If this value was below 0, the response size was set to 0 pA. If the value was larger than 0, we interpreted it as average drug response amplitude including failures and thus did not scale it. This conservative method prevents false negatives due to lacking sensitivity in individual trials in the presence of the drug.

Detection of spontaneous activity Spontaneous IPSCs were recorded prior to wash-in of DNI, in the presence of DNI and in the presence of each pharmacological compound. For each condition, data were analysed for a total duration of 20 s of recordings.

Analysis of afterhyperpolarizations All stable MC AP recordings within either baseline or drug condition were averaged (n = 5 each). If between the two conditions the holding membrane potential changed by more than 0.3 mV, or the time course (onset of upstroke relative to onset of step depolarization, width) and/or the amplitude of the AP changed by more than 15% from their baseline values, the experiment was discarded. If single individual recordings showed such variations, they were not included in the average. For each average, the AHP amplitude was measured as the maximal negative deflection of the membrane potential from the resting membrane potential.

Simulations

The simulations are based on a published compartmental model in NEURON (Aghvami et al., 2019, ModelDB entry 244687). This model uses the 5-state gating model for NMDA receptors (*Destexhe et al. 1998*), while the HVACC model is adopted from *Hemond et al. 2008,* with adjustments based on own Ca^{2+} current recordings (see *Aghvami et al. 2019*). For the simulations shown in Fig. 5, there was no exogenous Ca^{2+} buffer included except for panel E where fluorescence transients were simulated in the presence of 100 µM of the Ca^{2+}-sensitive dye OGB-1 in order to emulate the experimental situation from *Bywalez et al. 2015*.

As a readout measure for the temporal overlap between I_{Ca_NMDAR} and I_{Ca_HVACC} we first determined the FWHM (full width half maximum) for each current and then the interval within which the two FWHMs overlapped. At this point, we focussed on temporal relationships and did not account for current amplitudes or integrals, since Ca^{2+} concentration changes within nanodomains cannot be properly simulated in NEURON and thus spine Ca^{2+} current amplitudes are of limited meaning. We tested for the robustness of this measure

against variation of those model parameters that are crucially involved in the generation of the spine spike, i.e. the resistance of the spine neck (R_{neck}), the conductance of AMPA receptors (g_{AMPA}) and the voltage-gated sodium channel conductance (varied in proportion to the potassium channel conductance, $g_{Na/K}$). Their nominal values in the GC model are 1.7 GΩ, 2000 pS and 0.5 S/cm^2 respectively. Each parameter was varied between up to 200% of the nominal value, and down until no spine spike was generated any more.

Immunogold labeling and electron microscopy

Immunogold labeling was performed on cryosubstituted rat olfactory bulbs (n = 4 animals, 3 months old), that had been used previously; for further details on the fixation, embedding and immunogold labeling procedure see (*Sassoè-Pognetto & Ottersen, 2000; Sassoè-Pognetto et al., 2003*).

To maximize detection of the GluN1 subunit, we used a combination of two rabbit antisera as described in *Sassoè-Pognetto et al. (2003)*. One antiserum (kindly donated by Anne Stephenson) binds an extracellular domain (amino acid residues 17–35) common to all splice variants of the GluN1 subunit (*Chazot et al. 1995; Racca et al. 2000*). The other antiserum was raised against a C-terminal domain and recognizes four splice variants (Chemicon, Temecula, CA; catalog No. AB1516).

For GluN2, we used a affinity-purified rabbit antibody raised against a synthetic peptide corresponding to the C-terminus of the GluN2A subunit conjugated to BSA (Chemicon, cat. no. AB1548). According to the manufacturer, this antibody recognizes the GluN2A and GluN2B subunits in Western blot analysis of transfected cells.

Ultrastructure data analysis and statistics

Grid squares were analysed systematically for the presence of synaptic profiles (symmetric and/or asymmetric) between GC spines and MC dendrites (Fig. 6; see also Fig. 1A in *Sassoè-Pognetto & Ottersen 2000*). Synaptic profiles were then photographed at high magnification (75.000 - 120.000x) with a side-mounted CCD camera (Mega View III, Olympus Soft Imaging System). The plasma membrane of GC spines, when clearly visible, was classified as either belonging to an asymmetric synaptic profile, a symmetric profile, or a non-synaptic segment (see Fig. 6A2 for examples). The length of segments was measured along the spine membrane curvature (using ImageJ 1.52 analysis software) and the number

of immunogold particles within a distance of ≤ 30 nm from the GC spine membrane was counted for the individual segments. The lengths of non-synaptic segments were on average longer than those of synaptic segments, which argues against an undersampling of gold particle densities in non-synaptic membranes compared to synaptic membranes and thus a false positive difference between the density distribution in non-synaptic membranes and symmetric profiles (GluN1: mean non-synaptic segment length: 610 ± 400 nm, n = 138, symmetric synaptic profiles: 270 ± 120 nm, n = 120, asymmetric synaptic profiles: 260 ± 110 nm, n = 111; similar results for GluN2, not shown). When both symmetric and asymmetric synaptic profiles were visible in the same individual spine, the distance of such reciprocal contacts was also measured along the curvature of the GC spine membrane.

The distribution of labeling along the axis perpendicular to the GC spine membrane (radial axis) was determined by examining micrographs of transversely cut synaptic profiles, with well defined presynaptic and postsynaptic membranes. Here all particles at distances up to 40 µm were counted to prevent a possible bias.

Statistical tests

All electrophysiological data were analysed with non-parametric paired (*Wilcoxon matched* pairs) or unpaired (*Mann-Whitney-U*) tests and expressed as mean ± SD. The density distributions of immunogold particles were compared with the Kolmogorov-Smirnov test (https://www.wessa.net/rwasp_Reddy-Moores%20K-S%20Test.wasp).

Author contributions

VLR performed all uncaging experiments. LZ performed MC current clamp recordings. VLR, GB, MSP and VE analyzed data. SSA performed simulations. VE and VLR designed research and wrote the manuscript, with MSP contributing to the parts on ultrastructure. BR provided DNI-caged glutamate and assisted in editing the manuscript.

Acknowledgments

We thank Anne Pietryga-Krieger for expert technical assistance, Marius Stephan and Philipp Seidel for assistance with IPSC analysis, Gagik Yeghiazaryan for initial MC current clamp recordings, Imre Vida for facilitating access to VGAT-Venus rats, Sigrun Korsching and Yoshiyuki Kubota for advice on statistics and Ursula Koch for advice on pharmacology and

967 discussions on lateral inhibition. This work was funded mainly by the German Federal
968 Ministry for Education and Research (BMBF, 01GQ1104/01GQ1502), with additional
969 equipment funding by LMU-GSN, DFG-SFB 870 and funding for staff from GIF (1479-418.13;
970 all to VE), and by ERC 682426, GINOP_2.1.1-15-2016-00979, VKSZ_14-1-2015-0155,
971 712821-NEURAM to BR.

972 ***Competing interests***

973 There are competing financial interests since BR is a founder of Femtonics Kft and a
974 member of its scientific advisory board. No other competing interests exist.

975

References

1. Abraham, N. M., Egger, V., Shimshek, D. R., Renden, R., Fukunaga, I., Sprengel, R., Seeburg, P. H., Klugmann, M., Margrie, T. W., Schaefer, A. T., & Kuner, T. (2010). Synaptic inhibition in the olfactory bulb accelerates odor discrimination in mice. *Neuron, 65*(3), 399-411.
2. Aghvami, S., Müller, M., Araabi ,B.N., & Egger V. (2019) Coincidence detection within the excitable rat olfactory bulb granule cell spines. *J. Neurosci*. 39, 584-595. doi: 10.1523/JNEUROSCI.1798-18.2018
3. Angelo, K., & Margrie, T. W. (2011). Population diversity and function of hyperpolarization-activated current in olfactory bulb mitral cells. *Sci Rep, 1*, 50. doi:10.1038/srep00050
4. Arevian A.,C., Kapoor, V., Urban, N.N. (2008). Activity-dependent gating of lateral inhibition in the mouse olfactory bulb. *Nat Neurosci* 11, 80-87.
5. Arnson, H. A., & Strowbridge, B. (2017). Spatial Structure Of Synchronized Inhibition In The Olfactory Bulb. *J Neurosci,* 37(43):10468 –10480. doi:10.1523/JNEUROSCI.1004-17.2017
6. Banerjee, A., Larsen, R.S., Philpot, B.D., & Paulsen,O. (2016). Roles of Presynaptic NMDA Receptors in Neurotransmission and Plasticity. *Trends in Neurosciences* 39 (1). http://dx.doi.org/10.1016/j.tins.2015.11.001
7. Bartel, D. L., Rela, L., Hsieh, L., & Greer, C. A. (2015). Dendrodendritic synapses in the mouse olfactory bulb external plexiform layer. *J Comp Neurol, 523*(8), 1145-1161. doi:10.1002/cne.23714
8. Beier KT, Kim CK, Hoerbelt P, Hung LW, Heifets BD, DeLoach KE, Mosca TJ, Neuner S, Deisseroth K, Luo L, Malenka RC. (2017) Rabies screen reveals GPe control of cocaine-triggered plasticity. Nature 549, 345-350. doi: 10.1038/nature23888.
9. Bloodgood, B. L., & Sabatini, B. L. (2007). Ca(2+) signaling in dendritic spines. *Curr Opin Neurobiol, 17*(3), 345-351. doi:10.1016/j.conb.2007.04.003
10. Bouvier, G., Bidoret, C., Casado, M., & Paoletti, P. (2015). Presynaptic NMDA receptors: Roles and rules. *Neuroscience, 311*, 322-340. doi:10.1016/j.neuroscience.2015.10.033
11. Brea JN, Kay LM, Kopell NJ. (2009). Biophysical model for gamma rhythms in the olfactory bulb via subthreshold oscilations. *Proc Natl Acad Sci U S A,* 106, 21954-9. doi: 10.1073/pnas.0910964106.
12. Burton SD. (2017). Inhibitory circuits of the main olfactory bulb. J Neurophysiol. 2017 Oct 1;118(4):2034-2051. doi: 10.1152/jn.00109.2017
13. Bywalez, W. G., Patirniche, D., Rupprecht, V., Stemmler, M., Herz, A. V. M., Pálfi, D., Rozsa, B., & Egger, V. (2015). Local Postsynaptic Voltage-Gated Sodium Channel Activation in Dendritic Spines of Olfactory Bulb Granule Cells. *Neuron, 85*(3), 590-601. doi:10.1016/j.neuron.2014.12.051
14. Carlson, G. C., Shipley, M. T., & Keller, A. (2000). Long-lasting depolarizations in mitral cells of the rat olfactory bulb. *J Neurosci, 20*(5), 2011-2021.
15. Chae H, Kepple DR, Bast WG, Murthy VN, Koulakov AA, Albeanu DF. (2019). Mosaic

representations of odors in the input and output layers of the mouse olfactory bulb. Nat Neurosci. 22:1306-1317. doi: 10.1038/s41593-019-0442-z.

16. Chazot, P.L., Cik, M., & Stephenson, F.A. (1995). An investigation into the role of N-glycosylation in the functional expression of a recombinant heteromeric NMDA receptor. Mol Membr Biol, 12,331-337.
17. Chen, W. R., Xiong, W., & Shepherd, G. M. (2000). Analysis of relations between NMDA receptors and GABA release at olfactory bulb reciprocal synapses. *Neuron, 25*(3), 625-633.
18. Chiovini, B., Turi, G. F., Katona, G., Kaszas, A., Palfi, D., Maak, P., Szalay, G., Szabo, M. F., Szabo, G., Szadai, Z., Kali, S., & Rozsa, B. (2014). Dendritic spikes induce ripples in parvalbumin interneurons during hippocampal sharp waves. *Neuron, 82*(4), 908-924. doi:10.1016/j.neuron.2014.04.004
19. Cleland TA, Sethupathy P. (2006) Non-topographical contrast enhancement in the olfactory bulb. BMC Neurosci. 24,7:7.
20. Crespo, C., Liberia, T., Blasco-Ibáñez, J.M., Nácher, J., & Varea, E. (2013). The circuits of the olfactory bulb. The exception as a rule. Anat Rec (Hoboken)., 296(9):1401-1412. doi: 10.1002/ar.22732.
21. Destexhe, A., Mainen, Z.F., & Sejnowski, T.J. (1998). Kinetic models of synaptic transmission. In: Methods in Neuronal Modeling (2nd edition; edited by Koch, C., & Segev, I.). MIT press, Cambridge, 1998, 1-25.
22. Duguid, I., & Smart, T.G. (2004) Retograde activation of presynaptic NMDA receptors enhances GABA release at cerebellar interneuton-Purkinje cell synapses. *Nat Neurosci*, 7(5), 525-533.
23. Duménieu, M., Fourcaud-Trocmé, N., Garcia, S., & Kuczewski, N. (2015). Afterhyperpolarization (AHP) regulates the frequency and timing of action potentials in the mitral cells of the olfactory bulb: role of olfactory experience. Physiol Rep, 3(5). pii: e12344. doi: 10.14814/phy2.12344.
24. Economo MN, Hansen KR, Wachowiak M (2016) Control of Mitral/Tufted Cell Output by Selective Inhibition among Olfactory Bulb Glomeruli. Neuron 91, 397-411.
25. Egger, V. (2008). Synaptic sodium spikes trigger long-lasting depolarizations and slow calcium entry in rat olfactory bulb granule cells. *Eur J Neurosci, 27*(8), 2066-2075.
26. Egger, V., Svoboda, K., & Mainen, Z. F. (2003) Mechanisms of lateral inhibition in the olfactory bulb: efficiency and modulation of spike-evoked calcium influx into granule cells. J Neurosci 23:7551–7559.
27. Egger, V., Svoboda, K., & Mainen, Z. F. (2005). Dendrodendritic synaptic signals in olfactory bulb granule cells: Local spine boost and global low-threshold spike. *J Neurosci, 25*, 3521-3530.
28. Egger, V., & Urban, N. N. (2006). Dynamic connectivity in the mitral cell-granule cell microcircuit. *Semin Cell Dev Biol, 17*(4), 424-432.
29. Fantana AL, Soucy ER & Meister M (2008) Rat Olfactory Bulb Mitral Cells Receive Sparse

Glomerular Inputs. Neuron 59, 802–814.

30. Friedman, D., & Strowbridge, B. W. (2000). Functional role of NMDA autoreceptors in olfactory mitral cells. *J Neurophysiol, 84*(1), 39-50. doi:10.1152/jn.2000.84.1.39
31. Fukunaga, I., Herb, J. T., Kollo, M., Boyden, E. S., & Schaefer, A. T. (2014). Independent control of gamma and theta activity by distinct interneuron networks in the olfactory bulb. *Nat Neurosci, 17*(9), 1208-1216. doi:10.1038/nn.3760
32. Geramita M, Urban NN. (2017) Differences in Glomerular-Layer-Mediated Feedforward Inhibition onto Mitral and Tufted Cells Lead to Distinct Modes of Intensity Coding. J Neurosci. 2017 Feb 8;37(6):1428-1438.
33. Glitsch, M., & Marty, A. (1999). Presynaptic Effects of NMDA in Cerebellar Purkinje Cells and Interneurons. J Neurosci, 19(2):511-519.
34. Grunditz, Å., Holbro, N., Tian, L., Zuo, Y., & Oertner, T.G. (2008). Spine Neck Plasticity Controls Postsynaptic Calcium Signals through Electrical Compartmentalization. J Neurosci 28:13457-13466.
35. Halabisky, B., Friedman, D., Radojicic, M., & Strowbridge, B. W. (2000). Calcium influx through NMDA receptors directly evokes GABA release in olfactory bulb granule cells. *J Neurosci, 20*(13), 5124-5134.
36. Hemond, P., Epstein, D., Boley, A., Migliore, M., Ascoli, G.A., & Jaffe, D.B. (2008). Distinct classes of pyramidal cells exhibit mutually exclusive firing patterns in hippocampal area CA3b. *Hippocampus* 18:411-424.
37. Huang, L., Garcia, I., Jen, H.-I., & Arenkiel, B. R. (2013). Reciprocal connectivity between mitral cells and external plexiform layer interneurons in the mouse olfactory bulb. *Frontiers in Neural Circuits, 7*. doi:10.3389/fncir.2013.00032
38. Isaacson, J. S. (1999). Glutamate spillover mediates excitatory transmission in the rat olfactory bulb. *Neuron, 23*(2), 377-384.
39. Isaacson, J. S. (2001). Mechanisms governing dendritic gamma-aminobutyric acid (GABA) release in the rat olfactory bulb. *Proc Natl Acad Sci U S A, 98*(1), 337-342.
40. Isaacson, J. S., & Strowbridge, B. W. (1998). Olfactory reciprocal synapses: dendritic signaling in the CNS. *Neuron, 20*(4), 749-761.
41. Jackowski A, Parnavelas JG, Lieberman AR. (1978) The reciprocal synapse in the external plexiform layer of the mammalian olfactory bulb. Brain Res. 1978 Dec 22;159(1):17-28. doi: 10.1016/0006-8993(78)90106-3.
42. Kaeser, P. S., & Regehr, W. G. (2014). Molecular mechanisms for synchronous, asynchronous, and spontaneous neurotransmitter release. *Annu Rev Physiol, 76*, 333-363. doi:10.1146/annurev-physiol-021113-170338
43. Kampa, B., Clements, J., Jonas, P., & Stuart, G.J. (2004) Kinetics of Mg2+ unblock of NMDA receptors: implications for spike-timing dependent synaptic plasticity. J Physiol, 556.2, 337-345.
44. Kapoor, V., & Urban, N. N. (2006). Glomerulus-specific, long-latency activity in the olfactory

bulb granule cell network. *J Neurosci, 26*, 11706-11719.

45. Kashiwadani H, Sasaki YF, Uchida N, Mori K. (1999) Synchronized oscillatory discharges of mitral/tufted cells with different molecular receptive ranges in the rabbit olfactory bulb. J Neurophysiol. 82(4):1786-92.
46. Kato, H. K., Gillet, S. N., Peters, A. J., Isaacson, J. S., & Komiyama, T. (2013). Parvalbumin-expressing interneurons linearly control olfactory bulb output. *Neuron, 80*(5), 10.1016/j.neuron.2013.1008.1036. doi:10.1016/j.neuron.2013.08.036
47. Kauer J.S. & Cinelli A.R. Are there structural and functional modules in the vertebrate olfactory bulb? *Microsc. Res. Tech.* **24**, 157-167(1993)
48. Kay, L. M. (2003). Two species of gamma oscillations in the olfactory bulb: dependence on behavioral state and synaptic interactions. *J Integr Neurosci, 2*(1), 31-44.
49. Khawaled, R., Bruening-Wright, A., Adelman, J. P., & Maylie, J. (1999). Bicuculline Block of Small-conductance Calcium-activated Potassium Channels. *Pflügers Archiv : Eur J Physiol.* **438** (3): 314–321. doi:10.1007/s004240050915.
50. Kim DH, Phillips ME, Chang AY, Patel HK, Nguyen KT, Willhite DC. (2011) Lateral Connectivity in the Olfactory Bulb is Sparse and Segregated. Front Neural Circuits. 25;5:5. doi: 10.3389/fncir.2011.00005.
51. Lagier, S., Carleton, A., & Lledo, P.-M. (2004). Interplay between Local GABAergic Interneurons and Relay Neurons Generates Gamma Oscillations in the Rat Olfactory Bulb. *J Neurosci*, 24(18):4382– 4392.
52. Laurent G., Wehr M. & Davidowitz H. (1996) Temporal representations of odors in an olfactory network. *J. Neurosci.* **16**, 3837-3847 (1996)
53. Lepousez, G., Csaba, Z., Bernard, V., Loudes, C., Videau, C., Lacombe, J., Epelbaum, J., & Viollet, C. (2010). Somatostatin interneurons delineate the inner part of the external plexiform layer in the mouse main olfactory bulb. *J Comp Neurol, 518*(11), 1976-1994. doi:10.1002/cne.22317
54. Lester, R.A., Clements, J.D.,Westbrook, G.L., & Jahr, C.E. (1990) NMDAR Channel kinetics determine the time course of NMDA receptor-mediated synaptic currents. Nature, 346(6284):565-567.
55. Li A., Gire H.G., & Restrepo D. (2015) Spike-Field Coherence in a Population of Olfactory Bulb Neurons Differentiates between Odors Irrespective of Associated Outcome. J Neurosci 35(14):5808-5822
56. Matsuno T, Kiyokage E, Toida K. (2017) Synaptic distribution of individually labeled mitral cells in the external plexiform layer of the mouse olfactory bulb. J Comp Neurol. 525(7):1633-1648. doi: 10.1002/cne.24148.
57. McGuinness, L., Taylor, C., Taylor, R.D., Yau, C., Langenhan, T., Hart, M.L., Christian, H., Tynan, P.W., Donnelly, P., & Emptage, N.J. (2010). Presynaptic NMDARs in the hippocampus facilitate transmitter release at theta frequency. *Neuron*, 68(6):1109-1127. doi: 10.1016/j.neuron.2010.11.023.

58. McIntyre, A. B. R., & Cleland, T. A. (2016). Biophysical constraints on lateral inhibition in the olfactory bulb. *Journal of Neurophysiology, 115*(6), 2937-2949. doi:10.1152/jn.00671.2015
59. McTavish TS, Migliore M, Shepherd GM, Hines ML. (2012) Mitral cell spike synchroniy modulated by dendrodendritic synapse location. Front Comput Neurosci. 6:3. doi: 10.3389/fncom.2012.00003.
60. Miller, J. P., Rall, W., & Rinzel, J. (1985). Synaptic amplification by active membrane in dendritic spines. *Brain Res, 325*(1-2), 325-330.
61. Miyamichi, K., Shlomai-Fuchs, Y., Shu, M., Weissbourd, B. C., Luo, L., & Mizrahi, A. (2013). Dissecting Local Circuits: Parvalbumin Interneurons Underlie Broad Feedback Control of Olfactory Bulb Output. *Neuron, 80*(5), 1232-1245. doi:10.1016/j.neuron.2013.08.027
62. Mori, K., Nagao, H., & Yoshihara, Y. (1999). The olfactory bulb: Coding and Processing of odor molecule information. *Science*, 286, 711-715.
63. Mueller M**.,** Egger V. (2020) Dendritic integration in olfactory bulb granule cells: Threshold for lateral inhibition and role of active conductances upon simultaneous activation. bioRxiv:901397. doi.org/10.1101/2020.01.10.901397
64. Nagayama S, Homma R, Imamura F. (2014) Neuronal organization of olfactory bulb circuits. Front Neural Circuits. 8:98. doi: 10.3389/fncir.2014.00098.
65. Najac M, Sanz Diez A, Kumar A, Benito N, Charpak S, De Saint Jan D. (2015) Intraglomerular lateral inhibition promotes spike timing variability in principal neurons of the olfactory bulb. J Neurosci. 35(10):4319-31. doi: 10.1523/JNEUROSCI.2181-14.2015.
66. Naritsuka, H., Sakai, K., Hashikawa, T., Mori, K., & Yamaguchi, M. (2009). Perisomatic-targeting Granule Cells in the Mouse Olfactory Bulb. *J Comp Neurol*, 525, 409-426.
67. Nunes, D., & Kuner, T. (2018). Axonal sodium channel NaV1.2 drives granule cell dendritic GABA release and rapid odor discrimination. *PLoS Biol, 16*(8), e2003816. doi:10.1371/journal.pbio.2003816
68. Pálfi, D., Chiovini, B., Szalay, G., Kaszás, A., Turi, G.F., Katona, G., Ábrányi-Balogh, P., Szőri, M., Potor, A., Frigyesi, O., Lukácsné Haveland, C., Szadai, Z., Madarász, M., Vasanits-Zsigrai, A., Molnár-Perl, I., Viskolcz, B., Csizmadia, I.G., Mucsi, Z., & Rózsa, B. (2018). High efficiency two-photon uncaging coupled by the correction of spontaneous hydrolysis. Org Biomol Chem. 16(11):1958-1970. doi: 10.1039/c8ob00025e.
69. Peace ST, Johnson BC, Li G, Kaiser ME, Fukunaga I, Schaefer AT, Molnar AC, Cleland TA (2017) Coherent olfactory bulb gamma oscillations arise from coupling independent columnar oscillations. bioRxiv 213827; doi: https://doi.org/10.1101/213827
70. Pressler, R. T., & Strowbridge, B. W. (2017). Direct Recording of Dendrodendritic Excitation in the Olfactory Bulb: Divergent Properties of Local and External Glutamatergic Inputs Govern Synaptic Integration in Granule Cells. *J Neurosci, 37*(49), 11774-11788. doi:10.1523/JNEUROSCI.2033-17.2017
71. Pressler, R. T., & Strowbridge, B. W. (2019). Functional specialization of interneuron dendrites: Identification of action potential initiation zone in axonless olfactory bulb granule

cells. J Neurosci. 39(49):9674-9688. doi: 10.1523/JNEUROSCI.1763-19.2019

72. Price J.L. & Powell T.P. (1970) An experimental study of the origin and the course of the centrifugal fibres to the olfactory bulb in the rat. *J Anat.* **107**:215-237
73. Racca, C., Stephenson, F.A., Streit, P., Roberts, J.D., & Somogyi, P. (2000). NMDA receptor content of synapses in stratum radiatum of the hippocampal CA1 area. J Neurosci. 20(7):2512-2522.
74. Rannals, M. D., & Kapur, J. (2011). Homeostatic strengthening of inhibitory synapses is mediated by the accumulation of GABA(A) receptors. *J Neurosci, 31*(48), 17701-17712. doi:10.1523/JNEUROSCI.4476-11.2011
75. Sailor, Kurt A., Valley, Matthew T., Wiechert, Martin T., Riecke, H., Sun, Gerald J., Adams, W., . . . Lledo, P.-M. (2016). Persistent Structural Plasticity Optimizes Sensory Information Processing in the Olfactory Bulb. *Neuron, 91*(2), 384-396. doi:http://dx.doi.org/10.1016/j.neuron.2016.06.004
76. Sassoé-Pognetto, M., & Ottersen, O. P. (2000). Organization of Ionotropic Glutamate Receptors at Dendrodendritic Synapses in the Rat Olfactory Bulb. J Neurosci, 20(6):2192–2201.
77. Sassoé-Pognetto, M., Utvik, J. K., Camoletto, P., Watanabe, M., Stephenson, F. A., Bredt, D. S., & Ottersen, O. P. (2003). Organization of postsynaptic density proteins and glutamate receptors in axodendritic and dendrodendritic synapses of the rat olfactory bulb. *J Comp Neurol, 463*(3), 237-248.
78. Schmidt, L. J., & Strowbridge, B. W. (2014). Modulation of olfactory bulb network activity by serotonin: synchronous inhibition of mitral cells mediated by spatially localized GABAergic microcircuits. *Learn Mem, 21*(8), 406-416. doi:10.1101/lm.035659.114
79. Schoppa, N. E., Kinzie, J. M., Sahara, Y., Segerson, T. P., & Westbrook, G. L. (1998). Dendrodendritic inhibition in the olfactory bulb is driven by NMDA receptors. *J Neurosci, 18*(17), 6790-6802.
80. Schoppa NE (2006) AMPA/kainate receptors drive rapid output and precise synchrony in olfactory bulb granule cells. J Neurosci 26:12996-13006.
81. Shao Z, Puche AC, Liu S, Shipley MT. (2012) Intraglomerular inhibition shapes the strength and temporal structure of glomerular output. J Neurophysiol. 108(3):782-93. doi: 10.1152/jn.00119.2012.
82. Shepherd GM, Chen WR, Willhite D, Migliore M, Greer CA. (2007) The olfactory granule cell: From classical enigma to central role in olfactory processing. Brain Res Rev 55, 373-382
83. Sobczyk, A., Scheuss, V., & Svoboda, K. (2005). NMDA receptor subunit-dependent [Ca2+] signaling in individual hippocampal dendritic spines. *J Neurosci, 25*(26), 6037-6046. doi:10.1523/JNEUROSCI.1221-05.2005
84. Spruston, N. (2008). Pyramidal neurons: dendritic structure and synaptic integration. *Nat Rev Neurosci, 9*(3), 206-221. doi:10.1038/nrn2286
85. Stanley, E. F. (2016) The Nanophysiology of Fast Transmitter Release. *Trends Neurosci*. 39

(3). http://dx.doi.org/10.1016/j.tins.2016.01.005

86. Stroh O, Freichel M, Kretz O, Birnbaumer L, Hartmann J, Egger V (2012) NMDA-receptor dependent synaptic activation of TRPC channels in the olfactory bulb. *J Neurosci 32*: 5737–5746
87. Toida, K., Kosaka, K., Heizmann, C. W., & Kosaka, T. (1994). Synaptic contacts between mitral/tufted cells and GABAergic neurons containing calcium-binding protein parvalbumin in the rat olfactory bulb, with special reference to reciprocal synapses between them. *Brain Res, 650*(2), 347-352.
88. Tonnesen, J., & Nagerl, U. V. (2016) Dendritic Spines as Tunable Regulators of Synaptic Signals. *Front Psychiatry* 7:101. doi: 10.3389/fpsyt.2016.00101
89. Uematsu, M., Hirai, Y., Karube, F., Ebihara, S., Kato, M., Abe, K., . . . Kawaguchi, Y. (2008). Quantitative Chemical Composition of Cortical GABAergic Neurons Revealed in Transgenic Venus-Expressing Rats. *Cerebral Cortex, 18*(2), 315-330. doi:10.1093/cercor/bhm056
90. Urban N.N. & Arevian A.C. (2009). Computing with dendrodendritic syanpses in the olfactory bulb. *Ann. N.Y. Acad. Sci. 1*170: 264–269. doi: 10.1111/j.1749-6632.2009.03899.x
91. Veruki, M. L., Zhou, Y., Castilho, A., Morgans, C. W., & Hartveit, E. (2019) Extrasynaptic NMDA Receptors on Rod Pathway Amacrine Cells: Molecular Composition, Activation, and Signaling. *J Neurosci* 39: 627-650. Doi: 10.1523/JNEUROSCI.2267-18.2018
92. Wallace, J. L., Wienisch, M., & Murthy, V. N. (2017). Development and Refinement of Functional Properties of Adult-Born Neurons. *Neuron, 96*(4), 883-896.e887. doi:10.1016/j.neuron.2017.09.039
93. Wellis, D. P., & Kauer, J. S. (1993). GABAA and glutamate receptor involvement in dendrodendritic synaptic interactions from salamander olfactory bulb. *J Physiol, 469*, 315-339.
94. Wienisch, M., & Murthy, V. N. (2016). Population imaging at subcellular resolution supports specific and local inhibition by granule cells in the olfactory bulb. *Scientific Reports, 6*, 29308. doi:10.1038/srep29308
95. Willhite DC, Nguyen KT, Masurkar AV, Greer CA, Shepherd GM, Chen WR (2006) Viral tracing identifies distributed columnar organization in the olfactory bulb. PNAS 103:12592-12597.
96. Woolf, T. B., Shepherd, G. M., & Greer, C. A. (1991). Serial reconstructions of granule cell spines in the mammalian olfactory bulb. *Synapse, 7*(3), 181-192.
97. Zelano C, Mohanty A, Gottfried JA. (2011) Olfactory predictive codes and stimulus templates in piriform cortex. Neuron. 72(1):178-87. doi: 10.1016/j.neuron.2011.08.010.
98. Zhang, L., Huang, Y., & Hu, B. (2016). Olfactory experiences dynamically regulate plasticity of dendritic spines in granule cells of Xenopus tadpoles in vivo. *Scientific Reports, 6*, 35009. doi:10.1038/srep35009

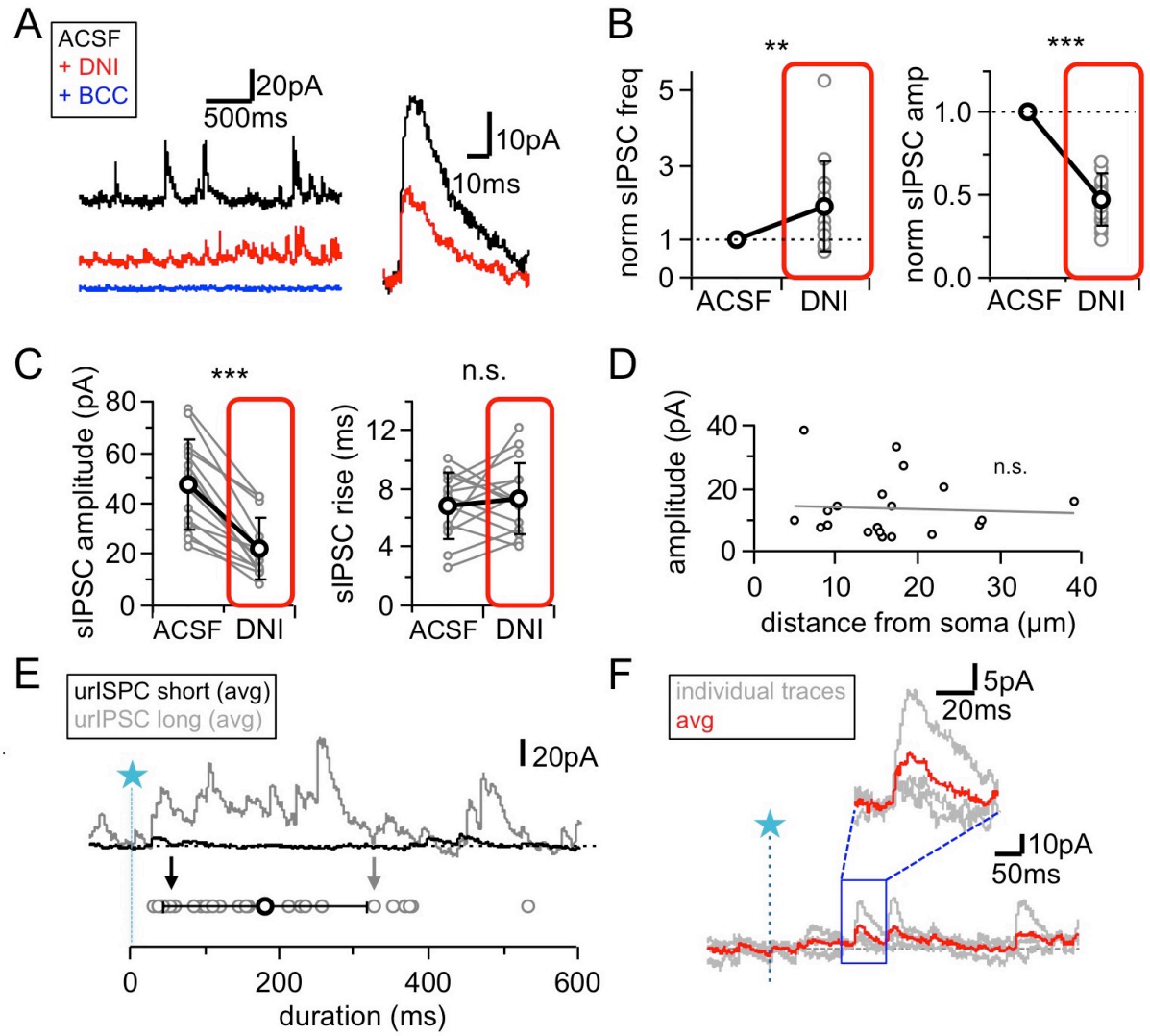

Figure S1. Effects of DNI (1 mM) on sIPSCs, uncaging sites, duration of responses

(**A**) Left: Example recordings in ACSF, after DNI wash-in and with added bicuculline (BCC, 50 µM). Right: Representative single events before and after DNI wash-in.

(**B**) Summary of effects of DNI (red) on spontaneous IPSCs. Left: Amplitude Right: Frequency (n = 14 MCs).

(**C**) Absolute changes in sIPSC parameters (amplitude, rise time) upon wash-in of DNI (red, n = 14).

(**D**) Distance of TPU site from soma versus urIPSC amplitudes. No correlation was found (n = 20).

(**E**) Top: Exemplary averaged responses from two experiments. Bottom: Cumulative durations of triggered events (black and grey arrow: durations of exemplary averaged responses).

(**F**) Exemplary experiment with a long latency of first detectable response (see Methods). Inset: Magnification of responses.